scientific reports

Check for updates

OPEN

Tailoring visible-light active TiO_2/cellulose nanocomposites with controlled crystalline structure for enhanced photocatalytic performance

Nutsupa Pimsawat[1], Somnuk Theerakulpisut[2] & Khanita Kamwilaisak[1]✉

This work involves a green and simple synthesis of TiO_2 nanoparticles on cellulose under mild conditions without the need for calcination via hydrolysis of titanium oxysulfate ($TiOSO_4$). The synthesis conditions, such as sulfuric acid concentration (0–10% wt), temperature (70–90 ℃), and time (4–8 h), focused on precisely controlling the structure of TiO_2 to enhance its photocatalytic effectiveness under visible light. At a lower 2.5 wt% sulfuric acid concentration, pure anatase was formed on the cellulose, while an increase in the range of 5.0–7.5 wt% sulfuric acid concentration yielded a rutile phase, resulting in a mixed phase of anatase and rutile on the cellulose. The pure rutile phase was found at a low temperature (70 ℃), while increased temperature led to the formation of the anatase phase. These results confirmed that the formation of crystalline TiO_2 phase on the cellulose depended on sulfuric acid concentration and temperature for hydrolysis. Additionally, the photocatalytic properties of the obtained materials were evaluated by degradationvisible of Rhodamine B (RhB) under UV and visible light. The findings revealed that the mixed phase (anatase/rutile) of TiO_2 on the cellulose demonstrated a superior photocatalytic efficiency (99.2%) compared to pure anatase (85.75%) and rutile (75.08%) when exposed to visible light.

Semiconductors are highly useful materials with high potential for many industrial applications such as energy and photocatalysis[1]. Photocatalysis of semiconductor can be used in the production of chemicals by degradation of biomass, and removal of pollution such as microplastic[2] and organic contamination[3] for water treatment. Among the semiconductors used for photocatalysis, titanium dioxide (TiO_2) has outstanding properties such as environmental friendliness, low cost, thermal and chemical stability and superior photocatalytic activity[1,3–7]. The photocatalytic efficiency of TiO_2 depends on its crystalline polymorph, morphology, particle size, and surface area[6,8].

In general, TiO_2 are available in three most commonly phases: anatase, rutile and brookite. Anatase and rutile phases have been reported in the literature more than brookite due to it's simplicity in synthesis. Moreover, anatase phase is the most reported for photocatalysis than rutile due to rutile having lower energy band gap causing inhibition of photocatalytic activity from fast recombination between the electrons and the holes. In addition, it is reported that a mixed-phase between anatase and rutile promotes greater photocatalytic activity more than only anatase phase, owing to efficient electron–hole separation from interconnection between anatase and rutile[3,9,10]. The best ratio between anatase and rutile for photocatalytic activity has been reported at 80:20[3,11] or 70:30[10], consistent with the ratio of mixed-phase TiO_2 in commercial grade, called Degussa P25, which is most used as a standard for evaluating photocatalytic activity of other photocatalysts. Therefore, synthesis of mixed-phase TiO_2 has received a great deal of research attention. The different phase ratio of TiO_2 depends on the method and condition for synthesis, especially temperature for calcination[6]. Normally, anatase phase was found in the initial period of synthesis after which the rutile phase was formed after an increase in calcination temperature (> 500 ℃), and eventually formation of only rutile phase was found (> 800 ℃)[12]. However, agglomeration of TiO_2 nanoparticles during the synthesis, storage, transportation and use was found to cause to a

[1]Department of Chemical Engineering, Faculty of Engineering, Khon Kaen University, Khon Kaen 40002, Thailand. [2]Energy Management and Conservation Office, Faculty of Engineering, Khon Kaen University, Khon Kaen 40002, Thailand. ✉email: khanita@kku.ac.th

decrease in photocatalytic efficiency. Moreover, due to the small particle size, recovery of the TiO_2 nanoparticles for reuse was difficult[4,5,7,13]. Consequently, immobilized particles on support were generally used in most studies to prevent the agglomeration.

Various materials such as biomass[14], polymer[15], glass fiber[16], wood[17] and cellulose[18] were used as supporting material of nanoparticles. Among supporting materials, cellulose is widely used due to its abundance, low cost and high hydroxyl content. Some research reported that hydroxyl groups on cellulose surface can act as a template to accelerate nucleation and growth of TiO_2 nanoparticles[7]. Moreover, cellulose can increase the absorption wavelength, resulting in an increase of photocatalytic efficiency. TiO_2 on cellulose was used in various applications such as adsorption, antibacterial activity[19], photodegradation[4], cosmetic[20] and energy storage[21]. Normally, the crystalline phase of TiO_2 was formed after calcination at higher than 400 ℃, but the temperature would degrade the cellulose support. Therefore, the process at low temperature for synthesis of TiO_2 nanoparticles was selected in this study.

A number of methods for synthesis of TiO_2 on cellulose support were reported such as dip coating[22], mixing[23], hydrothermal process[24], microwave irradiation[13] and hydrolysis[4,5,7,20,25]. Mixing is a simple method; however, it exhibited the lower interaction between cellulose and nanoparticles while the hydrothermal method required high temperature and specific equipment. Microwave irradiation has been used to reduce the reaction time but at a high cost of equipment. Among the processes, hydrolysis is considered attractive due to low temperature and requires no chemical agent. The popular precursor used for synthesis of TiO_2 on cellulose is titanium alkoxide such as titanium oxysulfate ($TiOSO_4$)[4,7,13,20], titanium (IV) isopropoxide (TTIP)[26] and titanium *n*-butoxide[27]. Among the alkoxide, $TiOSO_4$ is the most attractive due to low cost and ease of handling[7,28].

The factors which influence synthesis of TiO_2 by the hydrolysis process include temperature, acid concentration, precursor concentration and time. The temperature used by most researchers was between 70 and 110 ℃. The formation of crystalline phase of TiO_2 on cellulose was found to be pure anatase[4,25] and pure rutile[7], depending on temperature. Acid type also affects the formation of crystalline phase. Sulfuric acid (H_2SO_4) yields the anatase phase whereas hydrochloric acid (HCl) produces the rutile phase. The mixed phase can be obtained when nitric acid (HNO_3) is used[29,30]. However, pure anatase and rutile phase of TiO_2 with different H_2SO_4 concentration were reported by Shandilya and Capron. They found that at a lower concentration (0–0.03 M), no crystalline phase was formed while, between 0.03 and 0.15 M, the anatase phase of TiO_2 was generated, and between 0.15 and 0.4 M the rutile phase was formed[20]. Moreover, the mixed phase of TiO_2 on membrane from TTIP via low temperature dissolution precipitation and varying concentration of HCl, temperature and time was reported[10]. However, there has not been any report on the formation of mixed phase TiO_2 by hydrolysis of $TiOSO_4$ under sulfuric acid solution on cellulose in the literature.

In the present work, we report a facile method to synthesize TiO_2 on cellulose at low temperature and we obtained pure anatase, pure rutile and mixed phase of TiO_2 without post treatment. This method owns a number of advantages. The process is simple without hazardous chemicals, and low energy is consumed. The photocatalysis of as-synthesized TiO_2 for degradation of rhodamine B under UV and visible light was investigated. TiO_2 on cellulose also showed high efficiency for reusability. Moreover, the mechanism of rhodamine B degradation by the synthesized TiO_2 as a catalyst was studied in detail.

Materials and methods

Materials

Eucalyptus pulp was obtained from Phoenix Pulp and Paper (Public Company, Thailand). Titanium (IV) oxysulfate ($TiOSO_4$) and Rhodamine B were purchased from Sigma-Aldrich (Singapore). Analytical grade sulfuric acid (H_2SO_4, 96%), propan-2-ol ($(CH_3)_2CHOH$, 99.8%) and silver nitrate ($AgNO_3$, 99.8%) were supplied by R.C.I. Labscan (Thailand). L-Ascorbic acid was purchased from Fisher scientific (United Kingdom). Oxalic acid 2-hydrate was supplied by KEMAUS (Australia).

Preparation of TiO_2 on cellulose

A synthesis method of TiO_2 on cellulose substrate was modified from the method by Shandilya and Capron[20]. In brief, a mixture was prepared by combining 0.25 M of $TiOSO_4$ with 40 ml of sulfuric acid aqueous solution. Cellulose was obtained from *Eucalyptus* pulp. The *Eucalyptus* pulp was blended and sieved through an 80-mesh. The sieved pulp (0.5 g) was added to the mixture with continued agitation at a speed of 250 rpm at a reaction temperature of 70 ℃ for a reaction time of 4 h. The solution was then centrifuged and the residue was then washed with DI water until neutralized and then dried in an oven at 40 °C for 24 h. The influence of sulfuric acid aqueous concentration (0–10%), reaction temperature (70, 80 and 90 ℃), and reaction time (4, 6, and 8 h) on the phase structure of TiO_2 on cellulose was investigated. TiO_2 without cellulose was synthesized by using 0.25 M of $TiOSO_4$ with 40 ml of 5%H_2SO_4 at 90 °C for 8 h.

Characterization

The crystalline structure of all samples was determined by X-ray diffraction (XRD) (Bruker D8 Advance, Germany). The analysis was carried out using the scanning rate of 10°/min and 2θ in the range from 10° to 80°. The crystallinity index (%CrI) of cellulose was calculated following Eq. (1)[31].

$$\%CrI = \frac{I_{200} - I_{am}}{I_{200}} \quad (1)$$

where I_{200} is the maximum intensity of crystallinity plane 200 (2θ = 22.5°), while I_{am} is the intensity of amorphous structure (2θ = 22.5°).

The crystalline size of cellulose and cellulose-TiO_2 composites was calculated by Scherrer's and the value of the plane spacing (d-spacing) was calculated from Bragg's law[32]

Equation as follows:

$$L = \frac{K\lambda}{\beta cos\theta} \tag{2}$$

$$d = \frac{\lambda}{2Sin\theta} \tag{3}$$

where L is the crystalline size (nm), d is the value of plane spacing (Å), K is a dimensionless shape factor (K = 0.94), λ is the X-ray wavelength (λ = 0.15418 Å), β is half of the maximum intensity (FWHM), and θ is the Bragg angle.

The ratio of rutile phase was calculated by Spurr and Myers's method[3]:

$$W_R = \frac{1}{1 + 0.884\frac{I_A}{I_R}} \tag{4}$$

where I_A and I_R are integrated intensities of anatase (101) and rutile (110) diffraction peak, respectively.

Raman spectroscopy was used to confirmed the crystalline structure of all TiO_2 on cellulose samples. The spectra were detected by Raman Spectrometer (XploRA plus, Horiba, Kyoto, Japan) with a laser excitation wavelength of 532 nm.

The functional molecule group of all TiO_2 samples was analyzed by Fourier Transform Infrared Spectrophotometer (FTIR) (Bruker Tensor27 model, Germany). The sample was pressed into pellet form and measured at a resolution of 4 cm^{-1} with an accumulation of 32 scans. The results in the spectra range between 4000 and 500 cm^{-1} were recorded.

The particle size and crystalline structure (Phase) of all samples were detected by Transmission electron microscopy (TEM) and high-resolution TEM (HRTEM) (F.E.I., Model: TECNAI G2 20), respectively.

The morphology of all samples was analyzed using Field Emission Scanning Electron Microscopy (FE-SEM) (F.E.I., Model: Helios NanoLab G3 CX). The amount of elements on the sample was detected using this instrument by EDS.

Thermal stability of all samples was analyzed by thermal gravimetric analysis (DTG 60, Shimadzu, Japan). In brief, the heating rate is 10 °C/min in a temperature range of ambient to 800 °C under a nitrogen gas flow rate of 60 ml/min.

The absorption and reflection of each sample were determined by UV–VIS–NIR Spectrophotometer (Shimadzu UV-3101(PC), Japan). $BaSO_4$ was used as the reference baseline for the absorption and reflection measurement. The spectrum wavelength was in the range of 200–800 nm. The reflection value of each sample was determined for the energy band gap by following the Kubelka–Munk method combined with the Tauc relation[33,34]:

$$(\alpha h\nu) = A(h\nu - E_g)^n \tag{5}$$

where α is absorption, h is the Plank's constant (6.626×10^{-34} J s), ν is the frequency of photons, A is a proportionality constant, E_g is the average band gap of the material and n = 1/2 for indirect transmission. The indirect average bandgap transition energies were estimated from the intercepts of the linear portion of the $(\alpha h\nu)^{1/2}$ versus hν plots.

Photoluminescence spectra of all TiO_2 samples were measured on a photoluminescence (Multichannel spectrometer, Avantes) with LED laser under excitation at 255 nm.

The change of chemical structure by photocatalytic reaction of RhB was determined by NMR technique. All samples for ^{1}HNMR spectra were dried at 60 ℃ for 12 h and then dissolved in D_2O before measured by NMR (400 MHz) (Bruker, Model: Ascend-400 (Prodigy unit)).

Photocatalytic activity test

Photocatalytic activity of different crystalline TiO_2 on cellulose support under UV and visible light irradiation on Rhodamin B (RhB) degradation was determined. In the typical procedure, the catalyst (1 g/L) was added to a 50 mL aqueous solution of RhB dye (5 ppm). The mixture was agitated at a speed of 250 rpm in the dark for a time interval of 30 min to reach the adsorption–desorption equilibrium. Afterward, the mixture was irradiated using a lamp (Philips LED 18W) with an intensity of 6900 lx for visible light, while UV irradiation by using a UV lamp (Blacklight T5 8W, wavelength 365 nm (UVA)) with an intensity of 0.180 mW/m^2. Aliquots were collected from the photoreactor at a given time and then centrifuged to remove solid residues from the supernatant. The concentration of RhB in the supernatant was measured by UV–Vis spectrophotometer (Agilent Technologies, USA.). The degradation percentages, D % of the RhB dye were calculated using Eq. (6)[35]:

$$D(\%) = \frac{C_0 - C}{C_0} \times 100 \tag{6}$$

where C_0 is the initial concentration of the dye and C is the concentration at various times.

Batch recycle

An experiment was conducted to determine the remaining activity of cellulose-TiO_2 as a catalyst. The method was modified following that by Lin et al.[36]. The catalyst regeneration was carried out using the RhB solution volume based on the catalyst amount from the previous cycle. After the 1st cycle, the catalyst was separated by centrifuge at 5000 rpm, then washed with DI water and dried in an oven at 40 °C for 24 h. In the next cycle, the volume of RhB at 5 ppm was controlled by the weight of catalysts from the last cycle, and similar conditions were used for photodegradation.

Results and discussion

Effect of H_2SO_4 concentration on crystalline structure of TiO_2 on cellulose

TiO_2 on cellulose support was fabricated through an in situ hydrolysis process. Titanium oxysulfate is a precursor that can be dissolved in water and acidic conditions. Thus, the effect of H_2SO_4 concentration, ranging from 0 to 10% wt on the TiO_2 phase, was investigated by setting $TiOSO_4$ concentration, hydrolysis temperature, and time to be 0.25 M, 90 ℃, and 8 h, respectively.

Figure 1 shows the XRD pattern of TiO_2 on cellulose support at various H_2SO_4 concentrations. It is evident that the peaks corresponding to cellulose were observed in all samples at 2θ angles of 15.80° and 22.59°, indicating the presence of the (110) and (200) planes of cellulose type I[37]. The peak intensity at 2θ of 15.80° and 22.59° was increased with higher H_2SO_4 concentration. This suggested that the acidic condition not only preserved the crystalline structure of cellulose but also eliminated the amorphous regions. It was also observed that the peaks at 2θ of 25.30°, 38.11°, 47.96°, 54.54°, 62.61°, and 75.20° which represented (101), (004), (200), (105), (204), and (215) that referred to anatase phase TiO_2 in all the samples, except for TiO_2 on cellulose support at 5%wt and 7.5%wt of H_2SO_4. The new peaks were found at 2θ of 27.47°, 36.18°, and 41.20° which indicate (110), (101), and (111) of rutile phase. While at 10%wt of H_2SO_4, only the anatase phase of TiO_2 was found. A possible explanation that an increase of H_2SO_4 concentration affected to the crystalline phase of TiO_2 will be later discussed in the section which deals with the mechanism of TiO_2 formation on cellulose. The hydroxyl groups on cellulose could enhance the nucleation and growth of TiO_2 nanocrystals[7]. The crystalline size and percentage of anatase and rutile were calculated by Eqs. (2) and (4), with the results shown in Table 1. The percentage of rutile increased to nearly 10% when H_2SO_4 concentration was increased from 5 to 7.5%wt. The crystalline size of anatase and rutile were smaller in the range of 5.80–9.58 nm when compared with commercial TiO_2, of which crystalline size is more than 20 nm. The difference was due to the synthesis process in this research was without calcination. This result was consistent with the result of Shandilya and Capron[20]. To study the effects of temperature and time on the phase of TiO_2 from hydrolysis of $TiOSO_4$ on cellulose, we selected 5%H_2SO_4 and 10% H_2SO_4 concentration in the experiment.

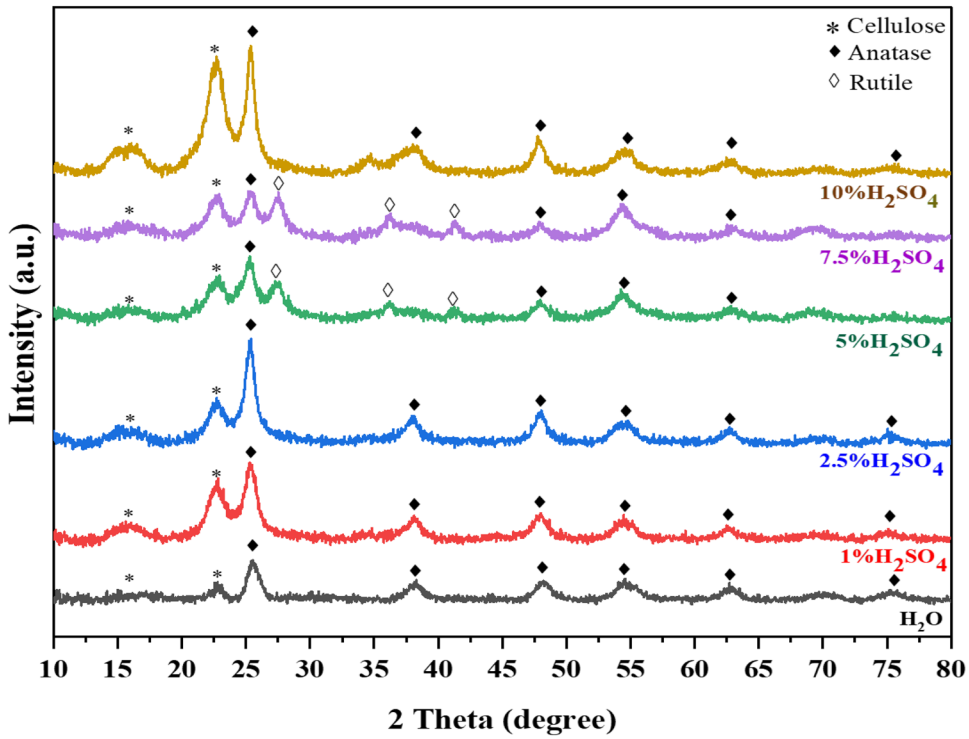

Figure 1. X-ray diffraction patterns of TiO_2 on cellulose with different H_2SO_4 concentration at 90 ℃ for 8 h.

Conditions	Ratio (%)		Crystalline size(nm)	
	Anatase	Rutile	Anatase	Rutile
H_2O	100		7.82	
$1\%H_2SO_4$	100		8.7	
$2.5\%H_2SO_4$	100		9.24	
$5\%H_2SO_4$	58.82	41.18	6.88	6.81
$7.5\%H_2SO_4$	48.43	51.57	6.46	7.43
$10\%H_2SO_4$ or cellulose-anatase	100		9.58	

Table 1. The ratio and crystalline size of anatase and rutile at different H_2SO_4 concentration.

Effect of temperature on the crystalline structure of TiO_2 on cellulose

The effect of temperature on the crystalline phase of TiO_2 on cellulose support at $5\%H_2SO_4$ and $10\%H_2SO_4$ is depicted in Figs. 2(a) and (b), respectively. In this study, the temperature was 70, 80, and 90 ℃ since it was desirable not to degrade the cellulose. The crystalline structure of cellulose was found to have similar peaks for all samples using $5\%H_2SO_4$ and $10\%H_2SO_4$ even though the temperature was varied from 70 to 90 ℃. On the contrary, the peak of TiO_2 significantly changed when the temperature increased from 70 to 90 ℃ at $5\%H_2SO_4$, as shown in Fig. 2(a). At 70 ℃, the peak appeared at 2θ of 27.57°, 36.32°, 41.63°, 54.49°, 56.72°, 63.41, and 69.58° which represent (110), (101), (111), (211), (220), (002) and (301) of the rutile phase[10]. Increasing the temperature to 80 ℃, a new small peak was detected at 2θ of 25.34° corresponding to (101) of the anatase phase. Finally, on increasing the temperature to 90 ℃, the peak at 25.34° was found to be higher than the peak at 27.40°. This result indicated that low acid concentration and low temperature were conducive to the formation of the rutile phase of TiO_2. In another case, at a high acid concentration ($10\%H_2SO_4$), the results are shown in Fig. 2(b). At low temperatures (70℃), no peak of crystalline TiO_2 was detected due to the complete dissolution of $TiOSO_4$ in $10\%H_2SO_4$[20]. In contrast, as evidenced in Fig. 2(b), increasing temperature to 80 and 90 ℃ caused the formation of crystalline anatase of TiO_2 on the cellulose. The percentage and crystalline size of anatase and rutile were calculated and shown in Table 2. It should be noted that the anatase phase was generated in an amount of 5% when the temperature increased from 70 to 80 ℃. At $5\%H_2SO_4$, the crystalline sizes of anatase and rutile were similar and found to be ~ 5–6 nm even though the hydrolysis temperature was different. Consistent with the result of Fischer et al.[10] and Björn Elgh & Anders E. C. Palmqvist[38], the result indicated that acid concentration and temperature played an important role in the formation of crystalline TiO_2.

Effect of Time on the crystalline structure of TiO_2 on cellulose

The last parameter of interest in the synthesis of TiO_2 in this work is reaction time. The reaction time was selected at 4, 6, and 8 h. The crystalline structure of TiO_2 and cellulose are shown in Figs. 3(a) and (b) for $5\%H_2SO_4$ and $10\%H_2SO_4$, respectively at 90 ℃. Figure 3(a) exhibited the peaks corresponding to anatase and rutile phases. When synthesis time was increased, the peaks remained similar for all the synthesis times but the intensity of anatase and rutile slightly changed. The ratio of anatase and rutile was calculated and shown in Table 3. The

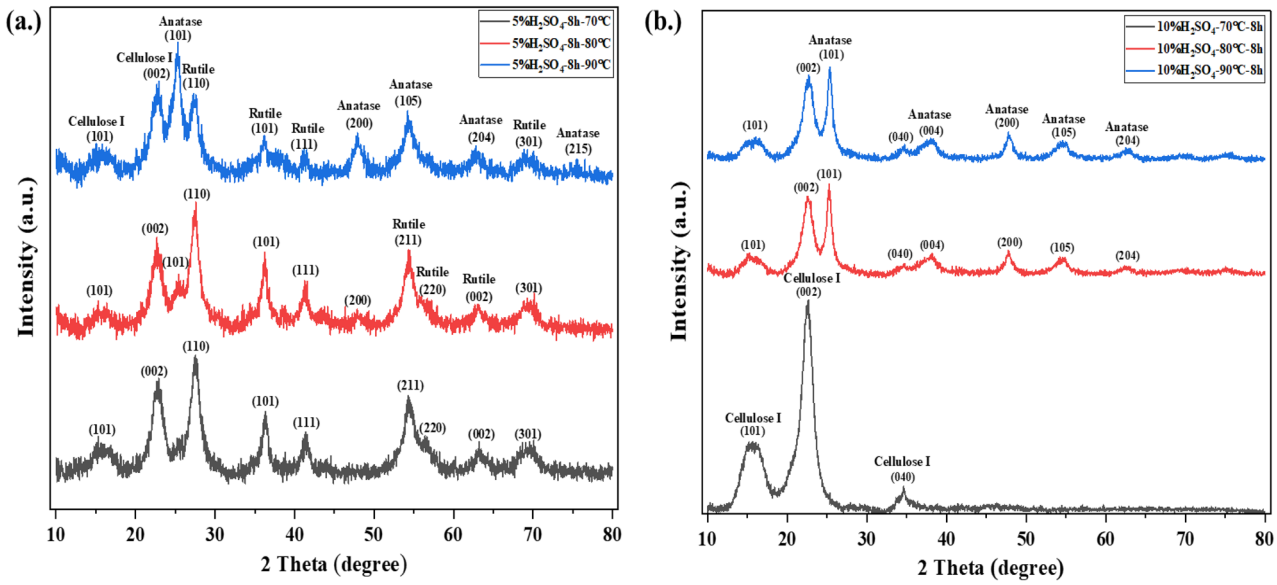

Figure 2. X-ray diffraction patterns of TiO_2 on cellulose at $5\%H_2SO_4$ (**a**) and $10\%H_2SO_4$ (**b**) at different temperatures.

Conditions	Ratio (%)		Crystalline size (nm)	
	Anatase	Rutile	Anatase	Rutile
5%H_2SO_4-70 ℃-8 h or cellulose-rutile		100		5.87
5%H_2SO_4-80 ℃-8 h	5.31	94.69	5.28	5.97
5%H_2SO_4-90 ℃-8 h or cellulose-mixed	58.82	41.18	5.8	5.68
10%H_2SO_4-70 ℃-8 h	N/A	N/A	N/A	N/A
10%H_2SO_4-80 ℃-8 h	100		10.54	

Table 2. Ratio and crystalline size of anatase and rutile at different temperature.

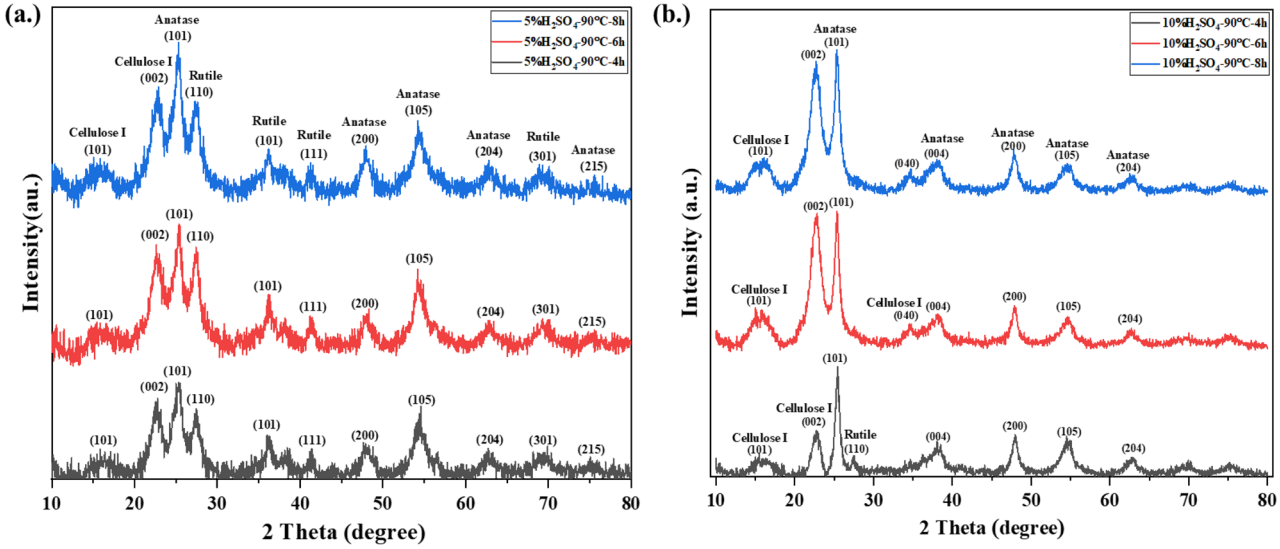

Figure 3. X-ray diffraction patterns of TiO_2 on cellulose at different time 5%H_2SO_4 (**a**) and 10%H_2SO_4 (**b**).

Conditions	Ratio (%)		Crystalline size (nm)	
	Anatase	Rutile	Anatase	Rutile
5%H_2SO_4-90 ℃-4 h	43.98	56.02	4.7	6.09
5%H_2SO_4-90 ℃-6 h	55.55	44.45	5.52	4.59
10%H_2SO_4-90 ℃-4 h	84	16	12.2	N/A
10%H_2SO_4-90 ℃-6 h	100		10.34	

Table 3. Ratio and crystalline size of anatase and rutile at different time.

percentage of rutile decreased from 56.02 to 41.18% when the reaction time increased from 4 to 8 h. In another condition at 10%H_2SO_4, and 90 ℃ the results are shown in Fig. 3(b). Similar and sharp peaks of anatase phase were found in all the samples regardless of reaction time. Only a small peak of rutile could be observed at 4 h.

To study the properties and efficiency of different phases of TiO_2 on cellulose, the samples obtained from various hydrolysis conditions, viz, 10% H_2SO_4, 90 ℃, 5% H_2SO_4 90℃ and 5%H_2SO_4, 70 ℃ for 8 h called cellulose-anatase, cellulose-mixed and cellulose-rutile, respectively, were investigated. The crystalline index, crystalline size and d-spacing of all the samples were calculated as shown in Table 4.

FTIR analysis

The functional groups of all samples were analyzed by FTIR and the results are shown in Fig. 4. The spectra of eucalyptus pulp contain many peaks including broad peaks at 3330 cm^{-1}, 2905 cm^{-1} and 1640 cm^{-1} which are related to O–H, C–H, and O–H stretching, respectively[39]. The sharp peak was exhibited at 1040 cm^{-1} which was associated with CO groups in the polysaccharide structure while the peaks at 1160 and 1104 cm^{-1} indicated C–O–C stretching[23]. These results confirmed that the eucalyptus pulp was cellulose type I[40]. The functional groups of TiO_2(P25) exhibited peaks at 500–800 cm^{-1} referring to Ti–O bond[41]. After the synthesis of different

Condition	Anatase		Rutile		Cellulose	
	Crystalline size (nm)	d-spacing (Å)	Crystalline size (nm)	d-spacing (Å)	CrI (%)	Crystalline size (nm)
Cellulose-anatase	9.58	3.51	–	–	88.46	5.31
Cellulose-mixed	5.80	3.53	5.68	3.25	78.02	5.03
Cellulose-rutile	–	–	5.87	3.24	74.72	5.17

Table 4. Crystalline size, crystallinity index of cellulose-TiO_2 polymorphs.

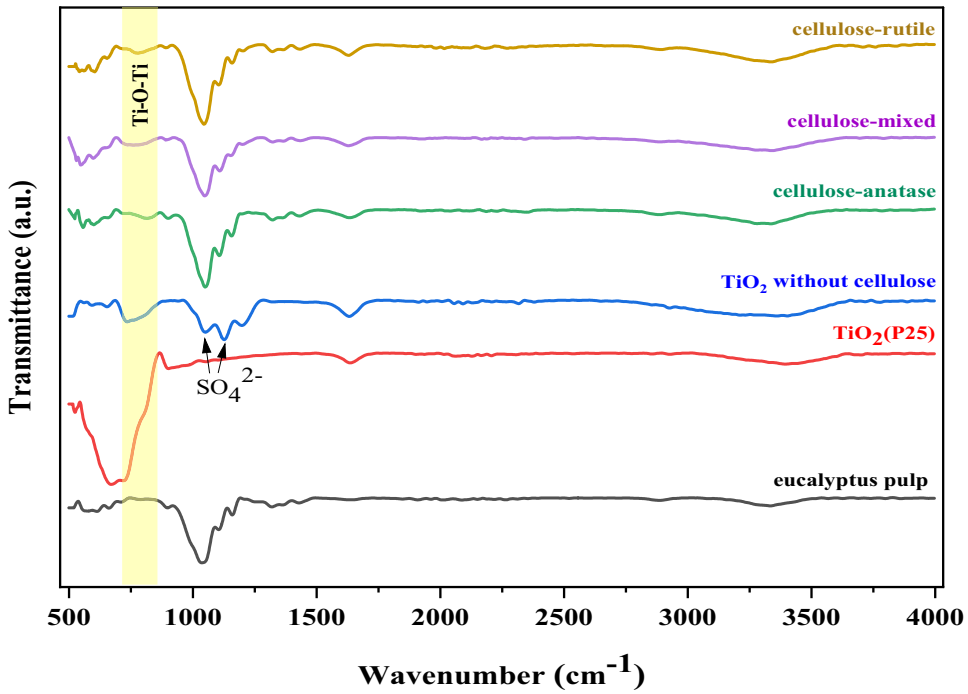

Figure 4. FTIR of TiO_2 on cellulose.

crystalline structure of TiO_2 on eucalyptus pulp, the spectra of cellulose exhibited similar peaks to those of eucalyptus pulp and TiO_2(P25) but a small peak of TiO_2 was observed on the samples due to low concentration of TiO_2 on eucalyptus pulp. Moreover, a new broad peak appeared at 810 cm^{-1} which correspond to Ti–O–Ti that was generated from the hydrolysis of $TiOSO_4$[42,43]. These results indicated that TiO_2 from hydrolysis adhered to cellulose in the eucalyptus pulp. The peaks at 1052 and 1127 cm^{-1} were observed in TiO_2 without cellulose which can be attributed to the characteristic of bidentate SO_4^{2-} coordinated to metals such as Ti^{4+}[44,45].

Raman spectroscopy

Since the FTIR spectra revealed only a small broad peak of TiO_2, Raman spectroscopy was used to confirm the existence of TiO_2 on the cellulose support. Moreover, the spectra in this technique can identify the crystalline phase of TiO_2. The results of Raman spectroscopy are shown in Fig. 5. TiO_2(P25) and eucalyptus pulp were used as control samples. The peaks of TiO_2 can be observed in the range of 100–1000 cm^{-1}. A sharp peak at 150–154 cm^{-1} was detected in cellulose-anatase, cellulose-mixed, and cellulose-rutile due to the spectra of the anatase phase and rutile phase being near one another[46]. Other peaks of cellulose-anatase were detected at 516 and 640 cm^{-1} while cellulose-rutile at 447 and 612 cm^{-1}[47]. Corresponding to the spectra of cellulose-mixed were observed broad peaks between 447 and 640 cm^{-1}. The results confirmed that different polymorphs of TiO_2 were formed on the cellulose by hydrolysis of $TiOSO_4$.

Mechanism for generating the crystalline structure of TiO_2 on cellulose

As previously mentioned, the H_2SO_4 concentration and temperature of the hydrolysis process significantly affect the generation of the crystalline TiO_2 phase on cellulose. A possible mechanism for the generation of the crystalline structure of TiO_2 on cellulose is shown in Fig. 6. $TiOSO_4$ reacts with water and H_2SO_4 to form $TiO(OH)_2$, the hydroxyl group on cellulose surface adsorbs $TiO(OH)_2$. $TiO(OH)_2$ nuclei then form by hydrolysis condensation, which subsequently grows into TiO_2 nanocrystals according to the following equations (7) and (8) [1]:

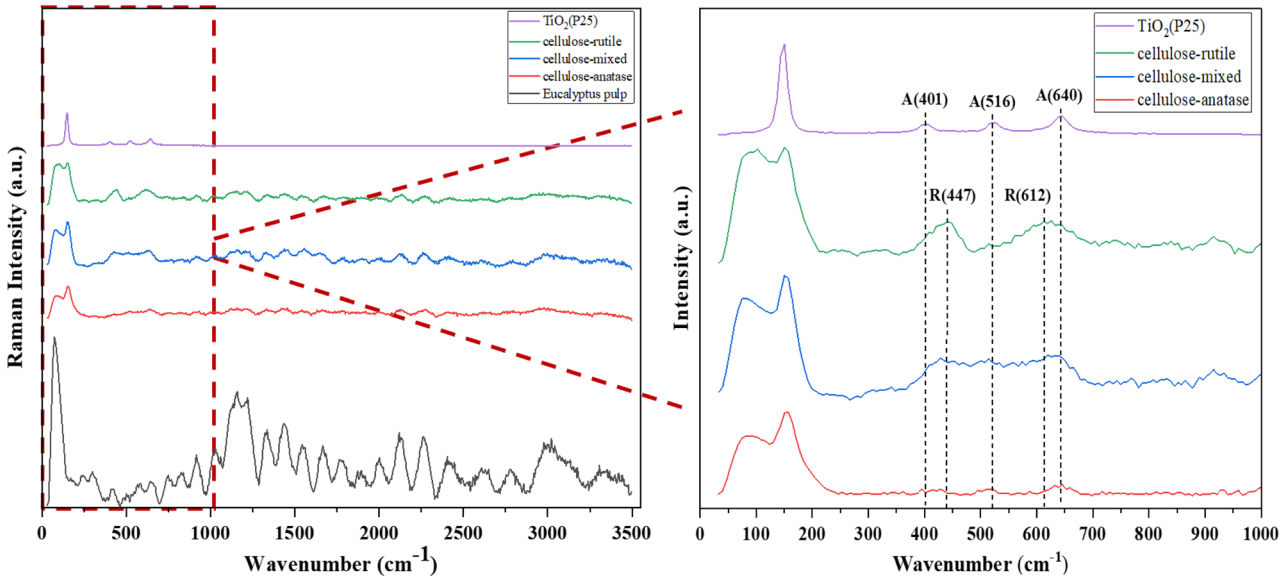

Figure 5. Raman spectroscopy of TiO_2 on cellulose.

$$TiOSO_4 + 2H_2O + H_2SO_4 \leftrightarrow TiO(OH)_2 + 2SO_4^{2-} + 4H^+ \quad (7)$$

$$TiO(OH)_2 \leftrightarrow TiO_2 + H_2O \quad (8)$$

Moreover, from Eq. (7) it can be seen that sulfuric acid will inhibit the formation of Ti–OH bonds, causing to slow down the hydrolysis reaction. Moreover, the heating rate in the dehydrating process could be a key factor in the arrangement of the TiO_2 crystalline.

TEM analysis

The structure and lattice spacing of TiO_2 immobilized on cellulose were characterized by TEM and HRTEM, respectively, as shown in Figs. 7(a), (b), and (c). As seen in the TEM images of all samples, the shape of cellulose was found in a rod-like shape and was observed to decrease in size due to the destruction of cellulose by sulfuric acid. Moreover, due to the drying process, agglomeration of the particles was observed[5]. TiO_2 particles appeared on the surface of the cellulose as black spots on the surface as shown in Figs. 7(a)–(c)[13]. The different phases of TiO_2 exhibited different distributions and densities. The well-distributed anatase of TiO_2 is shown in Fig. 7(a), while the clusters with higher density of mixed and rutile phases of TiO_2 were observed in Figs. 7(b) and (c), respectively. Nevertheless, these results confirmed that the TiO_2 was formed on the cellulose. The hydroxyl groups on cellulose were reported to be responsible for the nucleation of TiO_2 crystals[4]. The size of TiO_2 nanoparticles was found to be small and difficult to calculate for individual particles. Moreover, the particles tend to combine with neighboring particles by Ostwald ripening and grow into larger particles. This type of combination causes the mesoporous structure of TiO_2 on cellulose[1].

The HR-TEM was used to determine the lattice spacing for the identification of the crystalline phase of TiO_2. The lattice fringes with spacings of 3.47–3.48 Å in Fig. 7(a) can be ascribed to (101) plane of TiO_2 corresponding to the fringe distance of the anatase phase (3.46–3.52 Å)[48]. The lattice fringes with spacings of 3.24–3.26 Å in Fig. 7(c), which can be ascribed to the (110) plane, belonged to the rutile phase[49]. The lattice fringes with spacings 3.24 and 3.52 Å in Fig. 7(b) which are close to the (110) and (101) planes of rutile and anatase, respectively. These calculated results are consistent with the calculation of d-spacing from XRD results.

FE-SEM analysis

Morphology of eucalyptus pulp before and after immobilization of TiO_2 was observed by FESEM analysis, as shown in Figs. 8(a), (b), (c) and (d). Figure 8(a) is ascribed to the shape and surface of pure cellulose (eucalyptus pulp) before TiO_2 formation. The shape of cellulose was long chain fiber while the surface was rough. Figures 8(b), (c) and (d) show the shape and surface of cellulose after being doped with different TiO_2 crystalline phases from hydrolysis. On comparing the shape of cellulose, it was found that cellulose-anatase tended to be shorter than cellulose-mixed and cellulose-rutile because the cellulose-anatase was obtained by using high acid concentration (10%H_2SO_4), which caused destruction of the structure of cellulose by H^+ from the H_2SO_4.

Similar shapes and particle sizes of different TiO_2 polymorphs on cellulose are shown in Figs. 8(b2), (c2) and (d2). It is seen from these figures that small spherical particles of TiO_2 fully covered the surface of cellulose. The average particle sizes of TiO_2, which were calculated by image J program, were 47.24 ± 7.2, 41.82 ± 6.99 and 41.90 ± 5.16 nm for cellulose-anatase, cellulose-mixed and cellulose-rutile, respectively. In addition, it can also be seen the adherence between the TiO_2 particles causes the structure to be raspberry-like. As reported in other work, the hydroxyl group can promote the heterogeneous nucleation and growth of inorganic particles[4]. In our

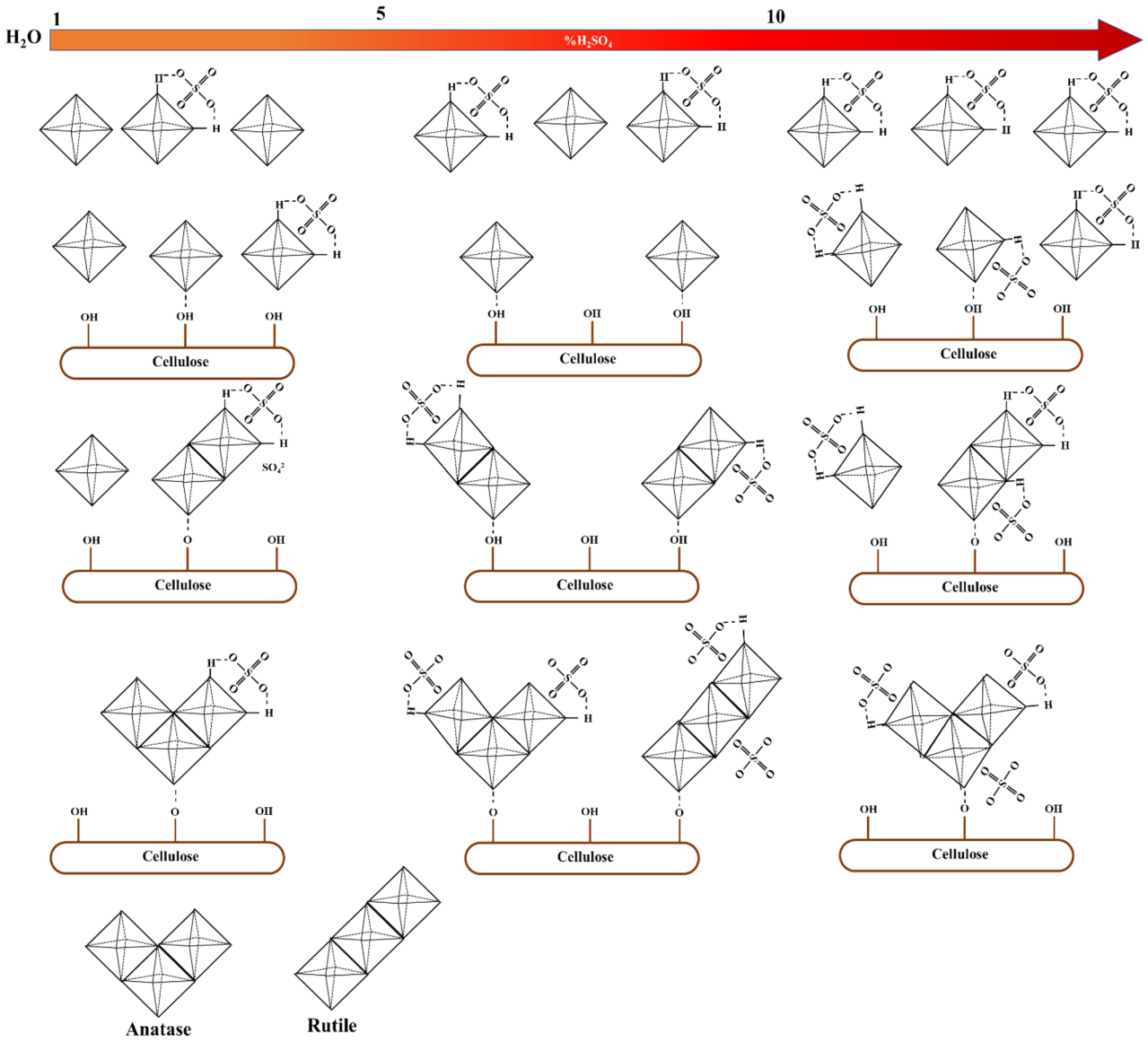

Figure 6. Proposed possible mechanism of the effect of H_2SO_4 concentration on the nucleation of TiO_2 crystalline structure on cellulose.

results, the hydroxyl groups on the cellulose surface acted as support for the formation of the primary nuclei of TiO_2 and subsequent growth into small crystals. The smaller crystals tend to combine into larger particles via Ostwald ripening to decrease the free surface energy[1].

TGA analysis

Thermal stability and amounts of immobilized TiO_2 nanoparticles on cellulose obtained from DTG analysis are shown in Fig. 9. Thermal degradation of eucalyptus pulp was detected in three stages. The first stage below 120 ℃ was attributed to the loss of water. High degradation was exhibited in the second stage which occurred between 250 and 380 ℃, normally referred to the decomposition of cellulose structure[13]. The final stage was the complete decomposition of cellulose. The degradation of cellulose-anatase, cellulose mixed and cellulose rutile had the same first stage but different in the second and third stages when compared with eucalyptus pulp. The decomposition took place between 200–350 ℃ and 350–500 ℃ for the second and the third stage, respectively. It should be noted that the second-stage decomposition temperature of cellulose was lower than that of eucalyptus. The lower temperature for the degradation of cellulose could be explained by the presence of H_2SO_4 in the system. The final weight from the TGA analysis indicated the amount of TiO_2 generated from hydrolysis of $TiOSO_4$ in percentage, numerically 36.35%, 33.13%, and 34.65% for cellulose-anatase, cellulose-mixed and cellulose-rutile, respectively. These results were comparable with those obtained from the EDS mapping of the percentage Ti element on the cellulose surface, as shown in FESEM images in Fig. 8.

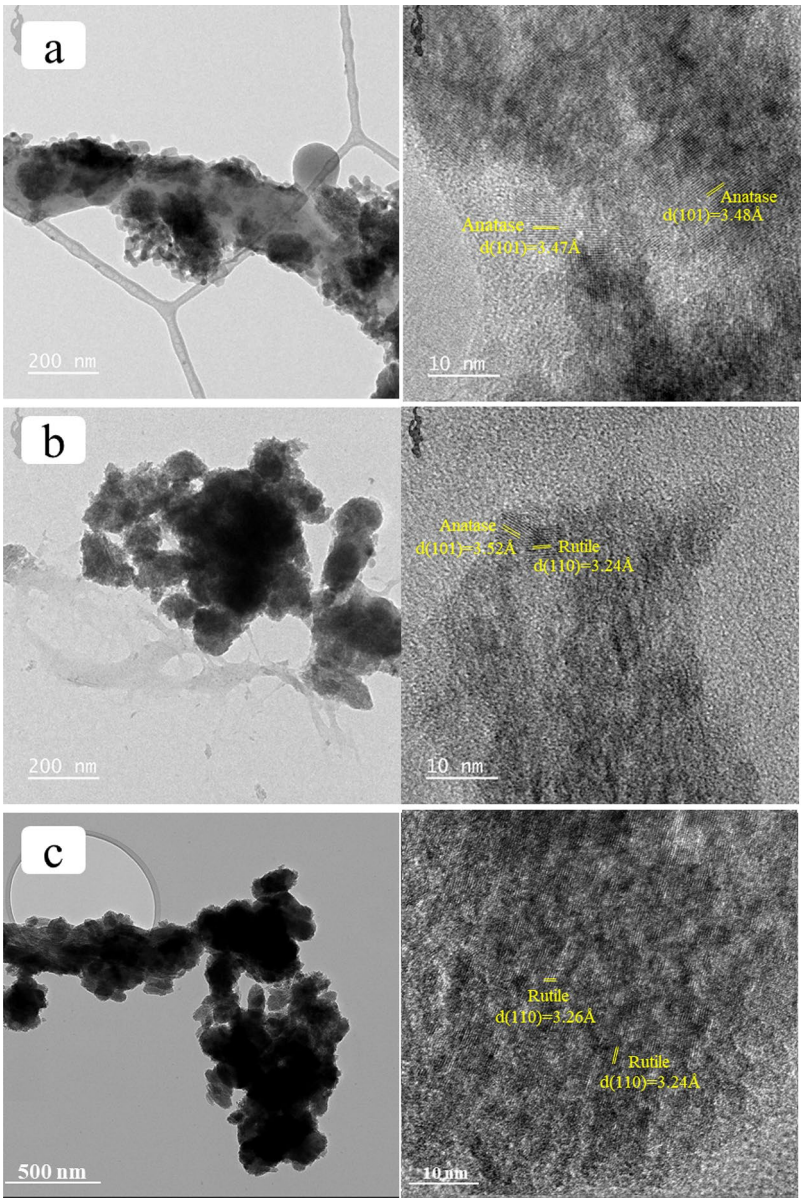

Figure 7. TEM images of cellulose-anatase (**a**), cellulose-mixed (**b**), and cellulose-rutile (**c**).

Photocatalytic activity

In other previous studies, low-temperature synthesis of TiO_2 on cellulose or nanocellulose by hydrolysis of $TiOSO_4$ found only pure anatase and pure rutile phases of TiO_2. The mixed phase of anatase and rutile can be obtained by calcination at high temperatures. In this study, we demonstrated a low-temperature synthesis to obtain mixed-phase TiO_2 on cellulose. To compare the efficiency of different phases of TiO_2 on cellulose in the photodegradation and kinetic reaction of rhodamine B, cellulose-anatase, cellulose mixed, and cellulose- rutile was tested under dark, UV illumination, and visible illumination conditions as shown in Figs. 10(a), (b), (c), (d) and (e), respectively.

Figure 10(a) illustrates the RhB adsorption of cellulose-anatase, cellulose-mixed, and cellulose-rutile after a duration of 180 min. The adsorption equilibrium was reached within the initial 30 min across all cellulose-TiO_2 structures. The cellulose-mixed exhibited the highest adsorption capacity, reaching 50%, whereas the cellulose-anatase and cellulose-rutile displayed approximately 16% and 18% adsorption, respectively.

Figures 10(b) and (c) depict the RhB photodegradation reaction of RhB, TiO_2(25), TiO_2 without cellulose, cellulose-anatase, cellulose mixed, and cellulose-rutile under UV and visible light. The adsorption was first tested in the dark to reach an equilibrium state before the initiation of the photodegradation reaction. It was seen that cellulose-mixed adsorbed RhB around 56%, which was higher than cellulose-anatase (42%) and cellulose-rutile (38%), for both UV and visible light. The adsorption of RhB on the cellulose-TiO_2 surface occurred by the electrostatic attraction between the negative charge from cellulose-TiO_2 and the positive charge from RhB. This

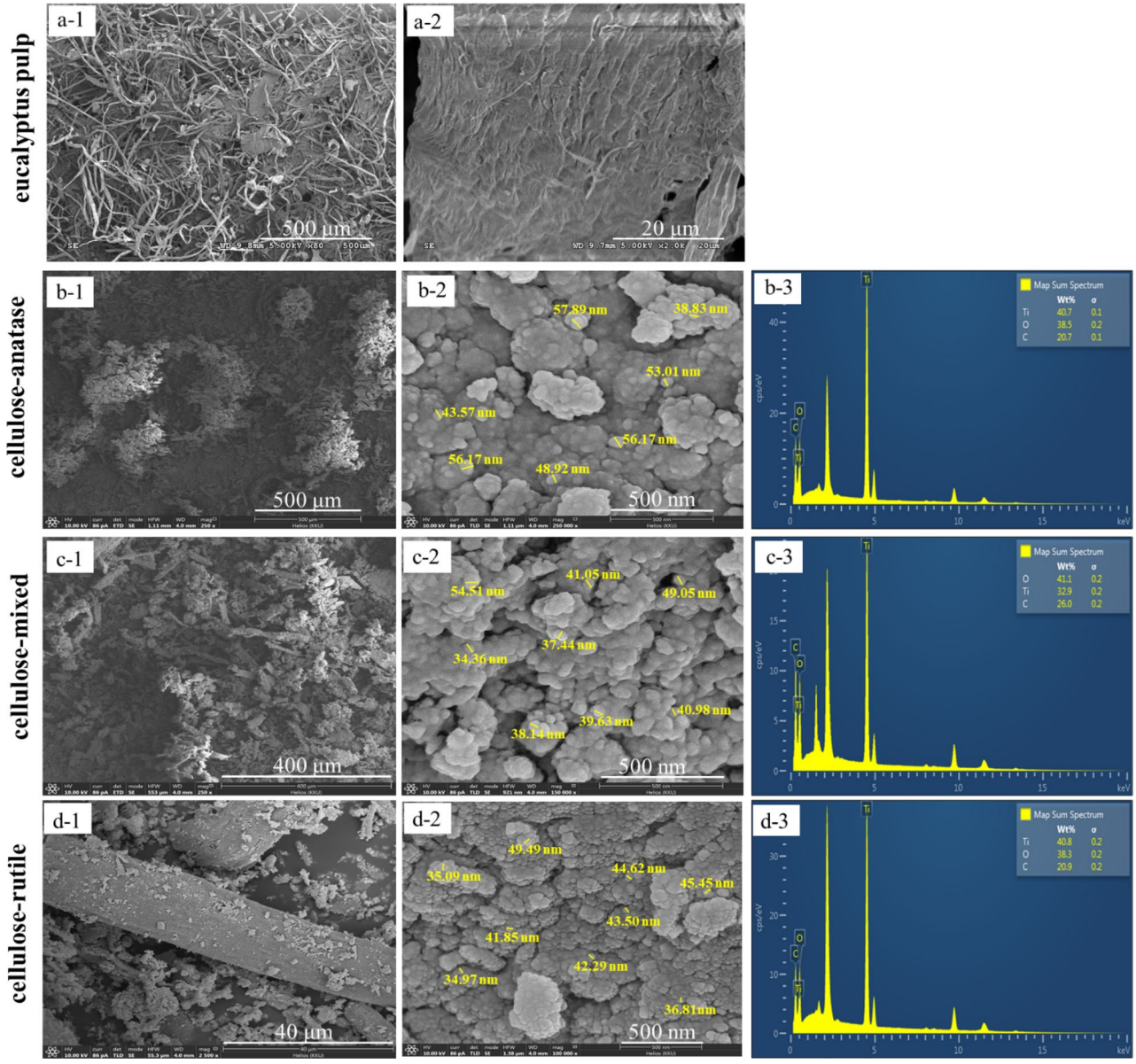

Figure 8. FESEM analysis of eucalyptus pulp (**a**), cellulose-anatase (**b**), cellulose-mixed (**c**) and cellulose-rutile (**d**).

result agreed with that reported by Carneiro et al.[50]. They reported that the positive charge of RhB occurred at the ethyl group while the benzine ring exhibited the negative charge. Moreover, the shape of cellulose-mixed exhibited more voids between particles than cellulose-anatase and cellulose-rutile, thus causing higher adsorption of RhB by the cellulose mixed.

The self-degradation of RhB by UV and visible light irradiation was 6% and 14%, respectively. The RhB removal efficiency of cellulose-anatase, cellulose-mixed, and cellulose-rutile reached 66.73%, 92.63%, and 45.62%, respectively, after 150 min exposure to UV light, as shown in Fig. 10(b). For visible light in Fig. 10(c), the degradation efficiency of RhB was found to be 85.75%, 99.2%, and 75.08% for cellulose-anatase, cellulose-mixed, and cellulose-rutile, respectively. It was evident that the crystalline phase of TiO_2 on the cellulose surface affected the efficiency of RhB degradation. The mixed phase between anatase and rutile exhibited better performance due to a lower energy band gap. Moreover, TiO_2 without cellulose (1 g/l) was used to confirm that cellulose can improve the efficiency of TiO_2. The degradation of RhB by TiO_2 without cellulose revealed around 93.59 and 89.62% efficiency for UV and visible light, respectively. These results indicated that TiO_2 on cellulose exhibited improved efficiency for RhB degradation in spite of the lower amount of TiO_2 in the system. Comparisons between the cellulose-mixed and commercial TiO_2(P25) under UV and visible light tests are shown in Figs. 10(b) and (c). The higher efficiency of cellulose-mixed than P25 was found under visible light, while both exhibited similar efficiency under UV light.

The first-order kinetics of RhB photodegradation under UV and visible light were computed and presented in Figs. 10(d) and (e), respectively. Additionally, the pseudo-first-order rate constant (k) was derived from the

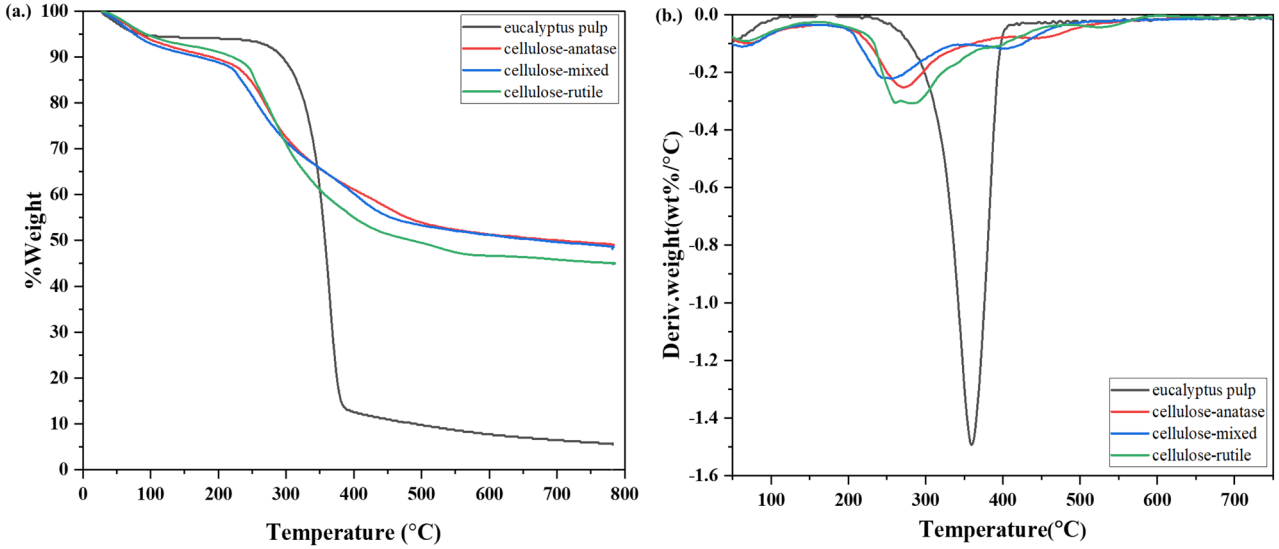

Figure 9. TGA (**a**) and DTG (**b**) analysis of eucalyptus pulp, cellulose-anatase, cellulose- mixed and cellulose-rutile.

slope of the line. The results indicate that the rate constant (k) for the cellulose-mixed is twice as high as that of cellulose-anatase and TiO_2 without cellulose in the degradation of RhB under visible light. Furthermore, Figs. 11(a) and (b) illustrate the UV–Vis spectrum of RhB after photodegradation by the cellulose-mixed structure under UV and visible light, respectively. The degradation efficiency of RhB under visible light with different processes and the impact of scavengers on RhB degradation by cellulose-mixed are presented in Figs. 11(c) and (d), respectively. Generally, the degradation of RhB under the photocatalytic process occurred by two pathways, namely cleavage of the whole conjugated chromophore and *N*-deethylation. In the cleavage of the chromophore, the main peak remained unchanged, but intensity decreased, while in the *N*-deethylation blueshifts of RhB peaks from 554 to 500 nm were detected by UV–Vis spectrometer[51].

A rapid shift of peak was seen from 554 to 498 nm after being exposed to visible light irradiation for 30 min. then the peak intensity was observed to decrease, as shown in Fig. 11(b). Under UV light, the shift of peak occurred from 554 to 532, 502, and 498 nm after exposure to the light for 30, 60, and 90 min, respectively. After that, a decrease in peak intensity was observed, as depicted in Fig. 11(a). These results indicated higher activity of cellulose-mixed structure under visible light than UV light. Pictures of the product after irradiation are shown in Figs. 11(a) and (b). Figure 11(c) displays the degradation efficiency of RhB by cellulose-mixed under different processes, including adsorption, photocatalytic, and adsorption & photocatalytic reaction. The maximum RhB degradation efficiency of 99.2% was obtained by adsorption and photocatalytic. However, RhB degradation by photocatalytic was 98.5% dye removal. Thus, the RhB degradation efficiency in both cases was similar, indicating that the key factor of the RhB degradation with cellulose-mixed was more the electronic structure (mixed phase) of TiO_2 than active adsorption sites.

The peak shifts explained the mechanism of RhB degradation when the cellulose-mixed was used as a catalyst. The first step was the adsorption of ethyl groups from RhB on the surface of the cellulose-mixed. After that, photocatalysis occurred by irradiation on the cellulose-mixed, and e^- from the valence band received more or equal energy to the energy bandgap; the e^- then went to the conduction band. At the valence band, h^+ reacted with water to generate the hydroxyl radicals ($OH^{\cdot}$), while e^- at the conduction band reacted with oxygen to form superoxide ($O_2^{\cdot -}$) according to the equations[52];

$$\text{Photoexcitation :cellulose-mixed} + h\upsilon\ (\text{visible}) \rightarrow e^- + h^+$$

$$\text{Oxidation :} h^+ + H_2O \rightarrow OH^{\cdot} + H^+$$

$$\text{Reduction :} O_2 + e^- \rightarrow O_2^{\cdot -}$$

$$\text{RhB} + OH^{\cdot} + O_2^{\cdot -} \rightarrow \text{photodegraded intermediates} \rightarrow H_2O + CO_2$$

After the degradation of the ethyl groups, the cleavage of the benzine ring[53] occurred until no peak of RhB was detected under UV–Vis, as shown in Figs. 11(a) and (b). This result confirmed that the complete degradation of RhB occurred when the cellulose-mixed was used as the photocatalyst.

Furthermore, a free radical scavenger test was conducted to explore the active species involved in RhB photodegradation. Isopropanol or propan-2-ol (IPA, 1:20 vol.) was introduced as the hydroxyl ($^{\cdot}OH$) radical scavenger[54], ascorbic acid (AA, 2 mM) as the superoxide ($^{\cdot}O^{2-}$) radical scavenger[55], oxalic acid (OA, 25 mM) as the hole (h^+)[56], and silver nitrate (SN, 100 mM) as the electrons (e^-)[57].

The scavenging experiments for reactive oxygen species mirrored the photodegradation test. Prior to photodegradation, the reactive oxygen species were added to the RhB solution before introducing the catalyst. Figure 11(d) illustrates the impact of radical scavengers on RhB photodegradation over the cellulose mixed using visible light.

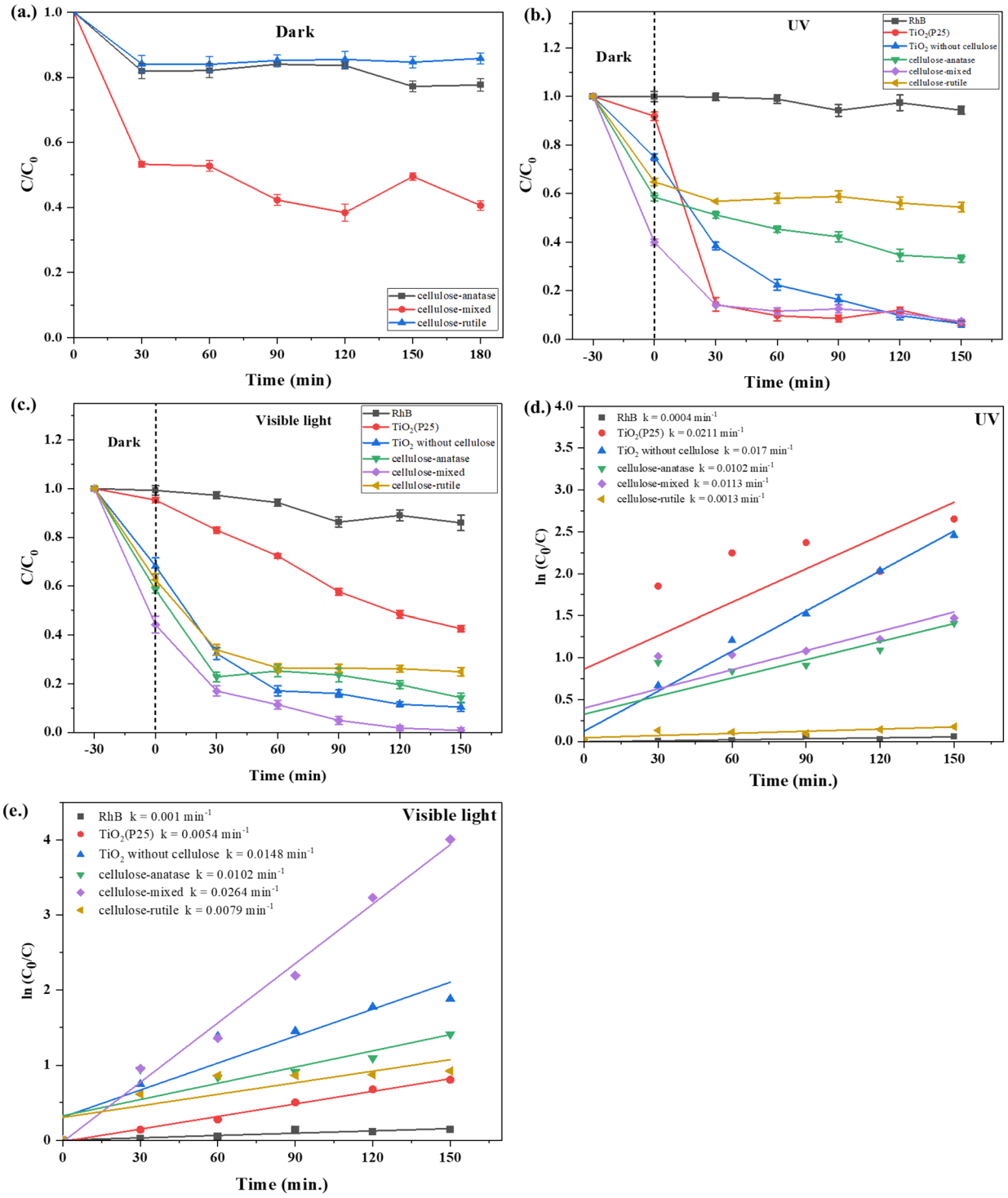

Figure 10. Degradation rate of RhB under (**a**) dark, (**b**) UV illumination, and (**c**) visible illumination, and the first-order kinetic plot of RhB under (**d**) UV illumination and (**e**) visible illumination.

As depicted in Fig. 11(d), the absence of any scavenger resulted in 99% removal of RhB, while 75% degradation was observed with SN, 74% with OA, and 72% with IPA, respectively. About 30% of RhB degradation was observed with AA. These findings indicate that $O_2^{\cdot-}$ plays a crucial role in RhB degradation, whereas $^{\cdot}OH$, h^+, and e^- have a relatively minor impact on the degradation process of RhB under visible light irradiation. Consequently, it can be inferred that superoxide is primarily responsible for the photodegradation of RhB.

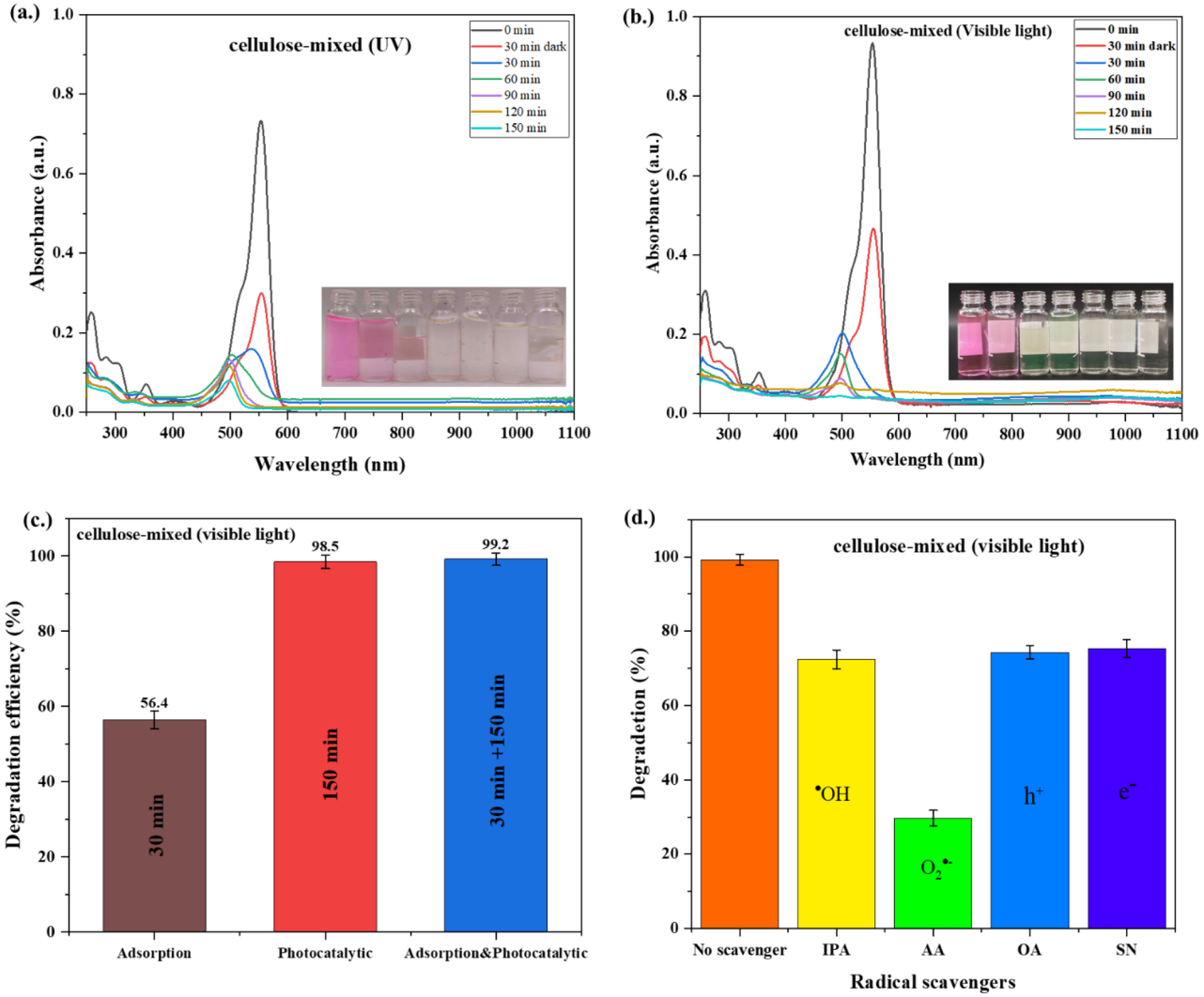

Figure 11. UV–Vis spectra of RhB solution as a function of (**a**) UV irradiation time and (**b**) visible irradiation time, (**c**) Degradation efficiency of RhB over cellulose-mixed under different processes and (**d**) radical scavengers on RhB photodegradation over the cellulose-mixed using visible light.

Energy bandgap

Optical properties of eucalyptus pulp, TiO_2(P25), TiO_2 without cellulose and cellulose-mixed were detected by UV–Vis DR, and the spectrum results are shown in Fig. 12 (a). It can be observed that the absorbance of the cellulose-mixed in the UV range between 200 and 400 nm was the highest as compared with commercial TiO_2(P25) and synthesized TiO_2 without cellulose. The stronger absorption in the visible light (400–800 nm) occurred in the eucalyptus pulp sample. As evidenced in Fig. 12(a), the absorption of radiation by TiO_2(P25) over a narrow wavelength range indicated that TiO_2(P25) was more active on UV rays than visible light. The higher absorbance of cellulose-mixed than that of the TiO_2 without cellulose in the visible region indicated that the cellulose-mixed also performed better under visible light for photocatalytic application. The energy band gap was determined by plotting the Kubelka–Munk function against the proton energy, as shown in Fig. 12(b). The band gap value of cellulose-mixed was found to be 3.08 eV, smaller than TiO_2 without cellulose (3.11 eV) and TiO_2(P25) (3.23 eV)[58]. This result confirmed that cellulose could enhance the performance of TiO_2 over a larger wavelength range, and the lower energy bandgap improved the photodegradation efficiency. Moreover, the performance of TiO_2 over a greater wavelength range and lower energy band gap of the cellulose mixed can also improve the efficiency of RhB degradation under visible light.

Photoluminescence analysis

It is well known that the energy band gap affects the photocatalytic efficiency. Moreover, the separation and transfer efficiency of photogenerated electron–hole pairs are the key factors of concern for photocatalytic activity[59]. The photoluminescence (PL) is a technique for probing the electronic structure, the transfer behavior of the photoexcited electron–hole pairs, and the rate of recombination of the material[60]. The recombination of photoexcited electron–hole pairs requires energy consumption, which increases the intensity of the spectrum, while

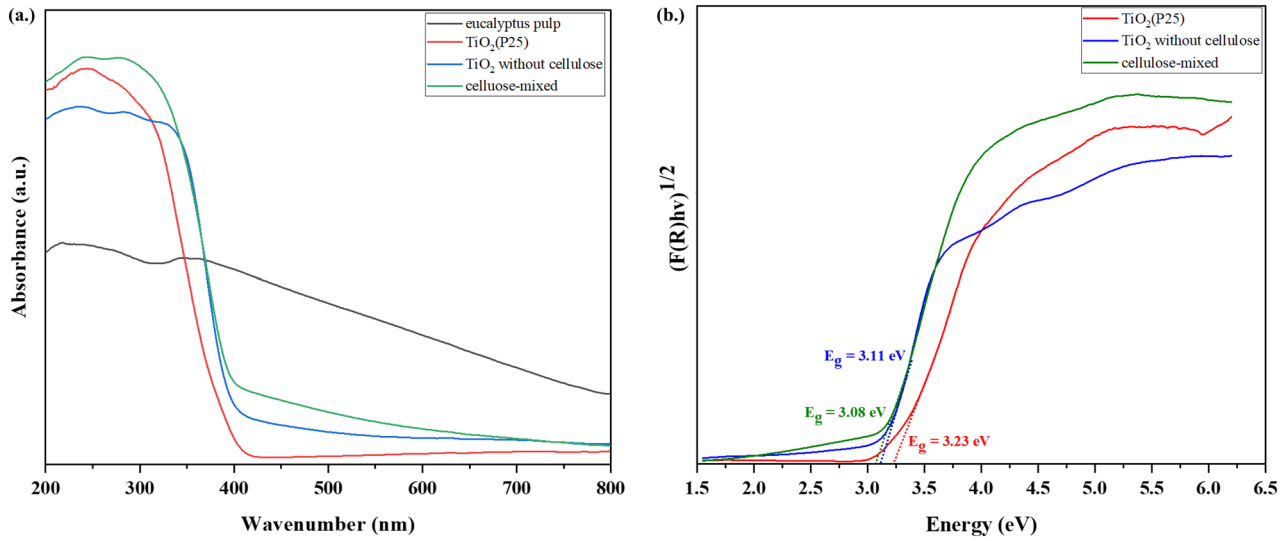

Figure 12. (**a**) UV–Vis DR spectra and (**b**) energy band gap values of eucalyptus pulp, TiO_2(P25), TiO_2 without cellulose and cellulose-mixed.

the lower PL intensity indicates a higher separation rate of photoinduced electron–hole pairs. This could be the advantage of photocatalytic activity[61]. PL spectra of eucalyptus pulp, TiO_2 without cellulose, TiO_2(P25), cellulose-anatase, cellulose-mixed, and cellulose-rutile are shown in Fig. 13. The PL spectra of all samples exhibited emissions peaks at 411 and 475 nm, which can be described as the self-trapped excitons in TiO_6 octahedral and the presence of oxygen vacancies in the TiO_2 nanoparticles, respectively[62]. The peak of eucalyptus pulp corresponds to a report by Yi Ding Chai et al. that the broad PL spectra of cellulose appeared at 450–650 nm[63]. The unique emission behaviors of cellulose were thought to originate from the electron-rich oxygen and/or glucose units, which also confirmed the aggregation-induced or crystallization-induced emissions from cellulose[63,64]. It can be seen that all the samples showed similar peaks of PL while the intensity of PL spectra tended to decrease when TiO_2 was immobilized on cellulose. The cellulose-mixed exhibited a lower PL intensity when compared with the cellulose-anatase and the cellulose-rutile. This result indicated that the cellulose-mixed had lower recombination of electron–hole pairs, which caused the electron and the hole to react with oxygen and water to produce highly reactive oxygen species that degraded pollutants via the oxidation processes[63,65]. The lower recombination of

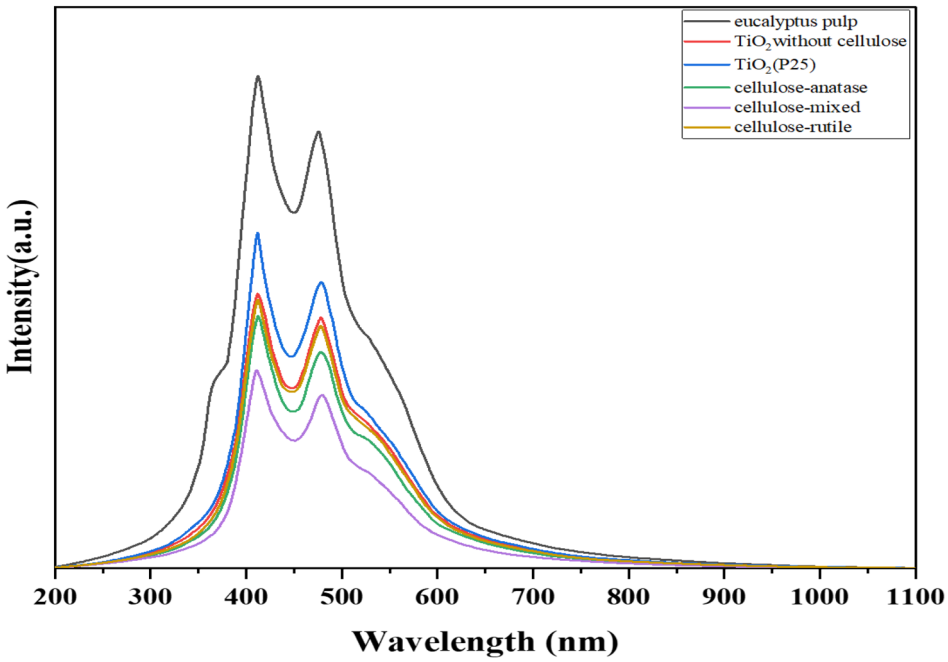

Figure 13. PL of eucalyptus pulp, TiO_2 (P25), TiO_2 without cellulose, cellulose-anatase, cellulose-mixed and cellulose-rutile.

the cellulose-mixed could be due to the mixed phase anatase and rutile causing a lower energy band gap, hence a higher photocatalytic activity of RhB degradation.

^{1}H NMR spectroscopy

To investigate the structure of RhB during the photocatalytic process, proton NMR analysis was performed. RhB solution after visible irradiation at 0, 30, 60, 90, and 120 min with the cellulose-mixed as catalyst was evaluated using ^{1}H NMR, and the results are shown in Figs. 14 (a)-(d). The broad and sharp peak appeared at

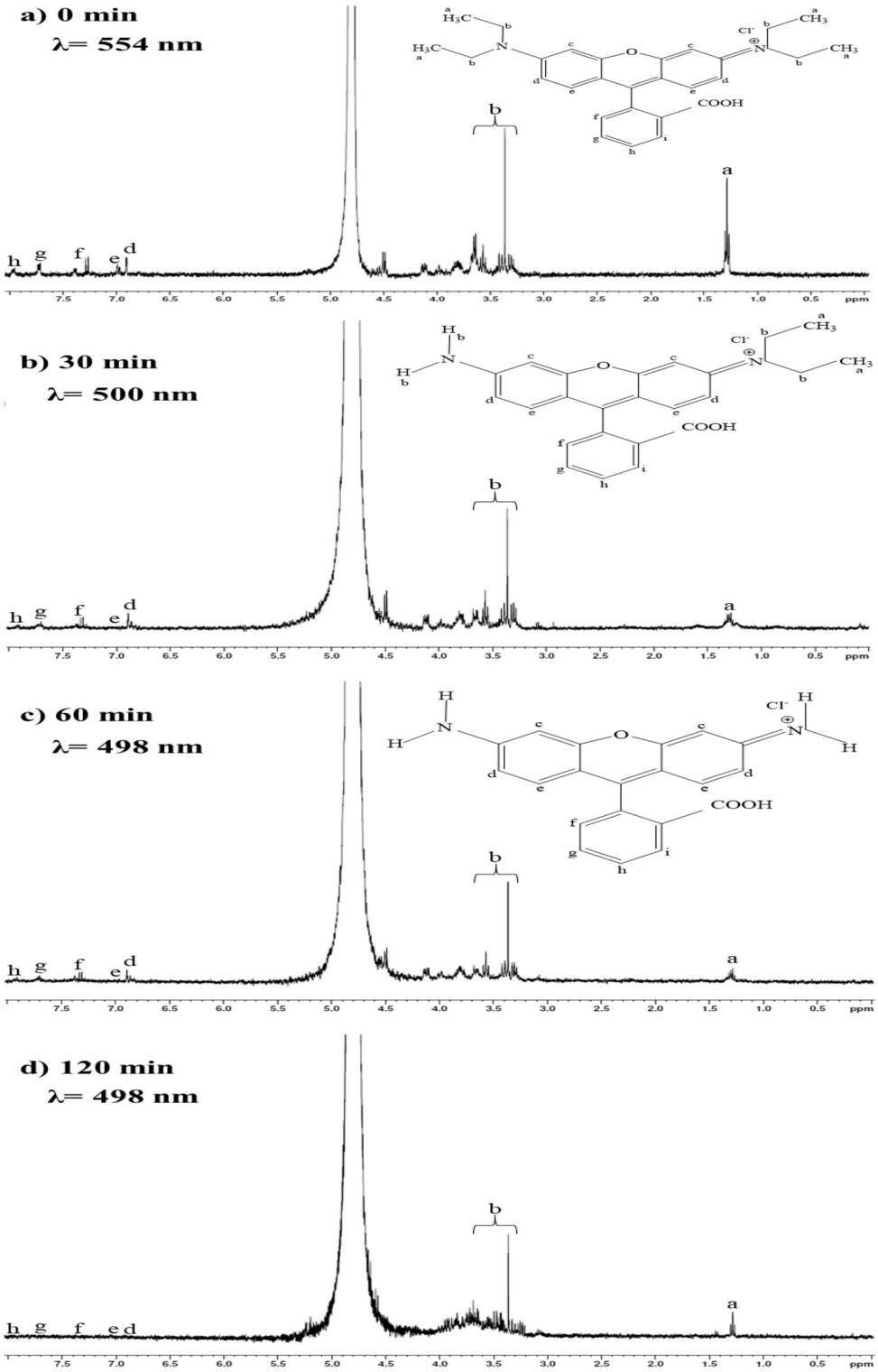

Figure 14. NMR spectrum of RhB at different degradation time.

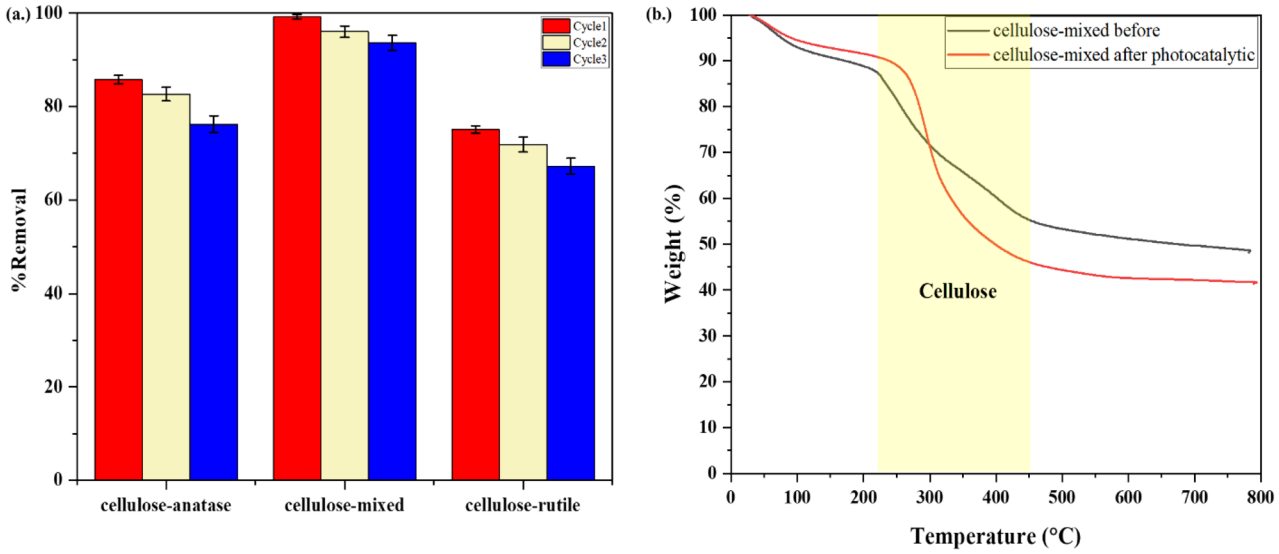

Figure 15. (**a**) Removal percentage of RhB by different catalysts under three cycles of visible light irradiation for 150 min and (**b**) TGA of cellulose-mixed before and after photocatalytic.

δ4.8 ppm, which indicated D_2O solvent. In the beginning, the ^1H NMR peaks of Ha and Hb of the ethyl groups were observed at δ1.30 ($-CH_3$) and 3.30–3.65 ppm ($-CH_2-$)[66]. The signal peaks of the aromatic hydrogen atoms Hd, He, Hf, Hg, Hh (d, e, f, g, and h referred to the H position in RhB structure) were exhibited at δ6.89, 6.95, 7.3, 7.7, and 7.9 ppm, respectively[67,68]. After 30 min irradiation, the peak of ethyl group at Ha was significantly decreased while that of Hb was slightly decreased. This result is consistent with the peak shift of UV–Vis from 554 to 498 nm to confirm the deethylation of RhB[69]. The decrease of aromatic hydrogen atom peaks was observed after irradiation of 60 min. After 120 min, no peak of the aromatic hydrogen atom was observed, indicating completion of RhB degradation. These NMR results indicated that the degradation of RhB under visible light by the cellulose-mixed occurred by the deethylation process at the initial stage of irradiation and then the breakup of chromophoric structure.

Reusability

Good photocatalysis, stability, and reusability are important for continuous use in photocatalytic applications. To evaluate the recycling performance of the as-prepared catalyst, cellulose-anatase, cellulose-mixed, and cellulose-rutile were tested by RhB degradation for three cycles under visible light. After each run, the catalyst without desorption was used in the next cycle, and the results are shown in Fig. 15(a). The regeneration efficiency of the cellulose-mixed was found to be more than 90% for RhB degradation after three cycles, while the regeneration efficiencies were 75% and 65% for the cellulose-anatase and the cellulose-rutile, respectively. These results indicate that the cellulose-mixed exhibited good stability and reusability due to many active sites to enhance the photocatalytic activity.

To confirm the photostability of cellulose, TGA analysis was used to determine the weight of cellulose[70] in the cellulose-mixed before and after photocatalytic reaction, as shown in Fig. 15(b). The result showed the weight of cellulose was increased from 45 to 55% due to the fact that cellulose could adsorb the residue RhB dye after 3 recycles of photocatalytic reaction. These results indicated that TiO_2 did not affect cellulose degradation.

Conclusions

The control of crystalline TiO_2 polymorphs on cellulose was successful by hydrolysis of $TiOSO_4$ at low temperatures. At lower H_2SO_4 concentrations (0–2.5%), the pure anatase phase was formed while an increase to 5–7.5% rutile phase occurred owing to the mixed phase of TiO_2 and increasing to 10% the pure anatase was found. The pure rutile phase was formed at 70 ℃ while increasing temperature, and the anatase phase appeared. The formation of the pure anatase phase and mixed-phase depended on the H_2SO_4 concentration, while pure rutile was found at low temperatures. Cellulose acted as the template to direct the crystal growth of TiO_2. The mixed phase of TiO_2 on cellulose showed the highest photocatalytic activity (92.63% and 99.2% for UV and visible light, respectively) when compared with pure anatase and rutile phase for degradation of RhB after 150 min exposure. The degradation mechanism of RhB by using TiO_2 on cellulose as a catalyst occurred by deethylation process. TiO_2 on cellulose exhibited good stability and reusability. This study provides a simple method to generate the crystalline phase of TiO_2, which exhibited a high potential catalyst for photodegradation without calcination in both UV and visible light systems. Additionally, it involves the customization of visible-light active cellulose-TiO_2 nanocomposites with controlled crystalline structures to enhance photocatalytic performance.

Data availability

The datasets used and/or analyzed during the current study available from the corresponding author on reasonable request.

Received: 6 November 2023; Accepted: 24 December 2023
Published online: 02 January 2024

References

1. Zhang, J., Li, L., Li, Y. & Yang, C. H_2SO_4 induced mesoporous TiO_2 nano-photocatalyst synthesized free of template under microwave. *Powder Technol.* **335**, 54–61 (2018).
2. Nabi, I. *et al.* Complete photocatalytic mineralization of microplastic on TiO_2 nanoparticle film. *iScience.* **23**, 101326. https://doi.org/10.1016/j.isci.2020.101326 (2020).
3. Wang, Q. *et al.* Hydrothermal synthesis and enhanced photocatalytic activity of mixed-phase TiO_2 powders with controllable anatase/rutile ratio. *Solid State Sci.* **77**, 14–19 (2018).
4. Li, Y. *et al.* Facile synthesis of TiO_2/CNC nanocomposites for enhanced Cr(VI) photoreduction: Synergistic roles of cellulose nanocrystals. *Carbohydr. Polym.* **233**, 115838. https://doi.org/10.1016/j.carbpol.2020.115838 (2020).
5. Zhan, C. *et al.* A study of TiO_2 nanocrystal growth and environmental remediation capability of TiO_2/CNC nanocomposites. *RSC Adv.* **9**, 40565–40576 (2019).
6. Kim, M. G. *et al.* Effects of Calcination temperature on the phase composition, photocatalytic degradation, and virucidal activities of TiO_2 nanoparticles. *ACS Omega.* **6**, 10668–10678 (2021).
7. Li, Y., Cao, L., Li, L. & Yang, C. In situ growing directional spindle TiO_2 nanocrystals on cellulose fibers for enhanced Pb^{2+} adsorption from water. *J. Hazard. Mater.* **289**, 140–148 (2015).
8. Khan, H. Sol–gel synthesis of TiO_2 from $TiOSO_4$: Characterization and UV photocatalytic activity for the degradation of 4-chlorophenol. *React. Kinet. Mech. Catal.* **121**, 811–832 (2017).
9. Li, H. *et al.* Facile phase control for hydrothermal synthesis of anatase-rutile TiO_2 with enhanced photocatalytic activity. *J. Alloys Compd.* **646**, 380–386 (2015).
10. Fischer, K. *et al.* Low-temperature synthesis of anatase/rutile/brookite TiO_2 nanoparticles on a polymer membrane for photocatalysis. *Catalysts.* **7**, 209 (2017).
11. Bagheri, S. & Julkapli, N. M. Mixed-phase TiO_2 photocatalysis: Correlation between phase composition and photodecomposition of water pollutants. *Rev. Inorg. Chem.* **37**, 11–28 (2017).
12. Phromma, S., Wutikhun, T., Kasamechonchung, P., Eksangsri, T. & Sapcharoenkun, C. Effect of calcination temperature on photocatalytic activity of synthesized TiO_2 nanoparticles via wet ball milling sol-gel method. *Appl. Sci.* **10**, 993 (2020).
13. Zhang, J., Li, L., Li, Y. & Yang, C. Microwave-assisted synthesis of hierarchical mesoporous nano-TiO_2/cellulose composites for rapid adsorption of Pb^{2+}. *Chem. Eng. J.* **313**, 1132–1141 (2017).
14. Luo, H. *et al.* Waste biomass-assisted synthesis of TiO_2 and N/O-contained graphene-like biochar composites for enhanced adsorptive and photocatalytic performances. *J. Alloys Compd.* **899**, 163287. https://doi.org/10.1016/j.jallcom.2021.163287 (2021).
15. Cazan, C., Enesca, A. & Andronic, L. Synergic effect of TiO_2 filler on the mechanical properties of polymer nanocomposites. *Polymers.* **13**, 2017 (2021).
16. Fukugaichi, S. Fixation of titanium dioxide nanoparticles on glass fiber cloths for photocatalytic degradation of organic dyes. *ACS Omega.* **4**, 15175–15180 (2019).
17. Xia, G. *et al.* Biomorphic porous TiO_2 with wood template size scaling for improved adsorption and photocatalysis performance. *Wood Sci. Technol.* **57**, 447–466 (2023).
18. Hamad, H. *et al.* 16-Cellulose–TiO_2 composites for the removal of water pollutants. in *Bio-Based Materials and Biotechnologies for Eco-Efficient Construction* 329–358 (Woodhead Publishing, 2020).
19. Zong, E. *et al.* Preparation of TiO_2/cellulose nanocomposites as antibacterial bio-adsorbents for effective phosphate removal from aqueous medium. *Int. J. Biol. Macromol.* **182**, 434–444 (2021).
20. Shandilya, N. & Capron, I. Safer-by-design hybrid nanostructures: An alternative to conventional titanium dioxide UV filters in skin care products. *RSC Adv.* **7**, 20430–20439 (2017).
21. Oh, S. I., Kim, J. C., Dar, M. A. & Kim, D. W. Synthesis and characterization of uniform hollow TiO_2 nanofibers using electrospun fibrous cellulosic templates for lithium-ion battery electrodes. *J. Alloys Compd.* **800**, 483–489 (2019).
22. Foruzanmehr, M., Vuillaume, P. Y., Robert, M. & Elkoun, S. The effect of grafting a nano-TiO_2 thin film on physical and mechanical properties of cellulosic natural fibers. *Mater. Des.* **85**, 671–678 (2015).
23. Ng, H. K. M. & Leo, C. P. The coherence between TiO_2 nanoparticles and microfibrillated cellulose in thin film for enhanced dispersal and photodegradation of dye. *Prog. Org. Coat.* **132**, 70–75 (2019).
24. Chauhan, I. & Mohanty, P. Immobilization of titania nanoparticles on the surface of cellulose fibres by a facile single step hydrothermal method and study of their photocatalytic and antibacterial activities. *RSC Adv.* **4**, 57885–57890 (2014).
25. Marques, P. A. A. P., Trindade, T. & Neto, C. P. Titanium dioxide/cellulose nanocomposites prepared by a controlled hydrolysis method. *Compos. Sci. Technol.* **66**, 1038–1044 (2006).
26. Cardoso, G. V. *et al.* Physico-chemical description of titanium dioxide–cellulose nanocomposite formation by microwave radiation with high thermal stability. *Cellulose* **25**, 2331–23419 (2018).
27. Chu, S. *et al.* Synthesis of uniform layer of TiO_2 nanoparticles coated on natural cellulose micrometer-sized fibers through a facile one-step solvothermal method. *Cellulose.* **26**, 4757–4765 (2019).
28. Khade, G. V., Suwarnkar, M. B., Gavade, N. L. & Garadkar, K. M. Green synthesis of TiO_2 and its photocatalytic activity. *J. Mater. Sci. Mater. Electron.* **26**, 3309–3315 (2015).
29. Jiang, X. *et al.* Low temperature synthesis and mechanism of finely dispersed nanorod rutile titanium dioxide. *RSC Adv.* **5**, 62160–62166 (2015).
30. Zhang, Z. G. *et al.* Influences of acids on morphology and properties of TiO_2 grown on electrospun PVDF fibers. *J. Phys. Chem. Solids.* **133**, 117–127 (2019).
31. Jutakridsada, P., Theerakulpisut, S., Srivastava, V., Sillanpää, M. & Kamwilaisak, K. Preparation and mechanism analysis of morphology-controlled cellulose nanocrystals by H_2SO_4 hydrolysis of Eucalyptus pulp. *Eng. Appl. Sci. Res.* **49**, 753–762 (2022).
32. Belardja, M., Djelad, H., Lafjah, M., Chouli, F. & Benyoucef, A. The influence of the addition of tungsten trioxide nanoparticle size on structure, thermal, and electroactivity properties of hybrid material-reinforced PANI. *Colloid Polym. Sci.* **298**, 1455–1463 (2020).
33. Alijani, M. & Kaleji, B. K. Optical and structural properties of TiO_2 nanopowders with Ce/Sn doping at various calcination temperature and time. *Opt. Quant. Electron.* **49**, 34 (2017).
34. Fonseca-Cervantes, O. R., Pérez-Larios, A. R., Arellano, V. H., Sulbaran-Rangel, B. & Guzmán González, C. A. Effects in band gap for photocatalysis in TiO_2 support by adding gold and ruthenium. *Processes.* **8**, 1032 (2020).
35. Chobchun, M. *et al.* Characterization of TiO_2-activated carbon onto adsorption and photocatalytic properties and its application. *J. Met. Mater.* **30**, 30–38 (2020).
36. Lin, Z., Lu, Y. & Huang, J. A hierarchical Ag_2O-nanoparticle/TiO_2-nanotube composite derived from natural cellulose substance with enhanced photocatalytic performance. *Cellulose* **26**, 6683–6700 (2019).
37. Jutakridsada, P. *et al.* Controllability, antiproliferative activity, Ag^+ release, and flow behavior of silver nanoparticles deposited onto cellulose nanocrystals. *Int. J. Biol.* **225**, 899–910 (2023).

38. Elgh, B. & Palmqvist, A. E. C. A facile low-temperature synthesis of TiO_2 nanoparticles with excellent polymorph control. *J. Sol.-Gel. Sci. Technol.* **76**, 395–401 (2015).
39. Zhang, C., Uchikoshi, T., Ichinose, I. & Liu, L. Surface modification on cellulose nanofibers by TiO_2 coating for achieving high capture efficiency of nanoparticles. *Coatings.* **9**, 139 (2019).
40. Rana, M. M. & De la Hoz Siegler, H. Influence of ionic liquid (IL) treatment conditions in the regeneration of cellulose with different crystallinity. *J. Mater. Res.* **38**, 328–336 (2023).
41. Tai, J., Leong, K., Pichiah, S., Abd Aziz, A. & Ching, S. Dopant-free oxygen-rich titanium dioxide: LED light-induced photocatalysis and mechanism insight. *J. Mater. Sci.* **52**, 11630–11642 (2017).
42. Galkina, O. L. *et al.* Antibacterial and photochemical properties of cellulose nanofiber–titania nanocomposites loaded with two different types of antibiotic medicines. *J. Mater. Chem. B.* **3**, 7125–7134 (2015).
43. Hussein, I. & Abdulrazzak, F. Preparation of TiO_2 nanoparticles using H_2O_2 /$TiOSO_4$ and applications in eosin yellow photocatalytic degradation. *NeuroQuantology.* **19**, 81–87 (2021).
44. Sun, B. *et al.* Spherical mesoporous TiO_2 fabricated by sodium dodecyl sulfate-assisted hydrothermal treatment and its photocatalytic decomposition of papermaking wastewater. *Powder Technol.* **56**, 118–125 (2014).
45. Huang, C.-W. *et al.* Solvothermal synthesis of mesoporous TiO_2 using sodium dodecyl sulfate for photocatalytic degradation of methylene blue. *Top Catal.* **63**, 1121–1130 (2020).
46. Monai, M., Montini, T. & Fornasiero, P. Brookite: Nothing new under the Sun?. *Catalysts.* **7**, 304 (2017).
47. Scrimieri, L. *et al.* Enhanced adsorption capacity of porous titanium dioxide nanoparticles synthetized in alkaline sol. *Appl. Phys. A.* **126**, 926 (2020).
48. He, J. *et al.* Facile formation of anatase/rutile TiO_2 nanocomposites with enhanced photocatalytic activity. *Molecules.* **24**, 2996 (2019).
49. Ambade, R. B. *et al.* Kinetically controlled low-temperature solution-processed mesoporous rutile TiO_2 for high performance lithium-ion batteries. *J. Ind. Eng. Chem.* **80**, 667–676 (2019).
50. Carneiro, J. O. *et al.* Visible light induced enhanced photocatalytic degradation of industrial effluents (rhodamine B) in aqueous media using TiO_2 nanoparticles. *J. Nanomater.* **2016**, 4396175. https://doi.org/10.1155/2016/4396175 (2016).
51. Chen, F., Zhao, J. & Hidaka, H. Highly selective deethylation of rhodamine B: Adsorption and photooxidation pathways of the dye on the TiO_2/SiO_2 composite photocatalyst. *Int. J. Photoenergy.* **5**, 674957 (2003).
52. Lee, S. Y., Kang, D., Jeong, S., Do, H. T. & Kim, J. H. Photocatalytic degradation of rhodamine B dye by TiO_2 and gold nanoparticles supported on a floating porous polydimethylsiloxane sponge under ultraviolet and visible light irradiation. *ACS Omega* **5**, 4233–4241 (2020).
53. Xi, J., Zhang, Y., Chen, X. & Hu, Y. A simple sol–gel hydrothermal method for the synthesis of defective TiO_2 nanocrystals with excellent visible-light photocatalytic activity. *Res. Chem. Intermed.* **46**, 2205–2214 (2020).
54. Santhosh, C., Malathi, A., Daneshvar, E., Kollu, P. & Bhatnagar, A. Photocatalytic degradation of toxic aquatic pollutants by novel magnetic 3D-TiO_2@HPGA nanocomposite. *Sci. Rep.* **8**, 15531 (2018).
55. Ali, M. E. M., Assirey, E. A., Abdel-Moniem, S. M. & Ibrahim, H. S. Low temperature-calcined TiO_2 for visible light assisted decontamination of 4-nitrophenol and hexavalent chromium from wastewater. *Sci. Rep.* **9**, 19354 (2019).
56. Adamu, H., McCue, A. J., Taylor, R. S. F., Manyar, H. G. & Anderson, J. A. Influence of pretreatment on surface interaction between Cu and anatase-TiO_2 in the simultaneous photoremediation of nitrate and oxalic acid. *J. Environ. Chem.* **7**, 103029. https://doi.org/10.1016/j.jece.2019.103029 (2019).
57. Trenczek-Zajac, A. *et al.* Scavenger-supported photocatalytic evidence of an extended type I electronic structure of the TiO_2@Fe_2O_3 interface. *ACS Appl. Mater. Interfaces.* **14**, 38255–38269 (2022).
58. Chokesawatanakit, N. *et al.* Ag-doped Cobweb-like structure of TiO_2 nanotubes for antibacterial activity against Methicillin-resistant Staphylococcus aureus (MRSA). *J. Environ. Chem.* **9**, 105843. https://doi.org/10.1016/j.jece.2021.105843 (2021).
59. Kavinkumar, V., Jaihindh, D. P., Verma, A., Jothivenkatachalam, K. & Fu, Y. P. Influence of cobalt substitution on the crystal structure, band edges and photocatalytic properties of hierarchical Bi_2WO_6 microspheres. *New J. Chem.* **43**, 9170–9182 (2019).
60. Ramesh, S., Kim, H. S. & Kim, J.-H. Cellulose-polyvinyl alcohol–nano-TiO_2 hybrid nanocomposite: Thermal, optical, and antimicrobial properties against pathogenic bacteria. *Polym. Plast. Technol. Eng.* **57**, 669–681 (2018).
61. Wan, J. *et al.* PDA/PEI-induced in-situ growth of a lotus leaf-like TiO_2 nanoparticle film on N-halamine cotton fabric for photocatalytic, self-cleaning and efficient antibacterial performance. *Cellulose.* **30**, 3953–3972 (2023).
62. Nabi, G., Raza, W. & Tahir, M. B. Green synthesis of TiO_2 nanoparticle using cinnamon powder extract and the study of optical properties. *J. Inorg. Organomet.* **30**, 1425–1429 (2020).
63. Chai, Y. D. *et al.* Role of oil palm empty fruit bunch-derived cellulose in improving the sonocatalytic activity of silver-doped titanium dioxide. *Polymers.* **13**, 3530 (2021).
64. Shanthini, G. M. *et al.* Surface stiffening and enhanced photoluminescence of ion implanted cellulose—Polyvinyl alcohol—Silica composite. *Carbohydr. Polym.* **153**, 619–630 (2016).
65. Sboui, M. *et al.* TiO_2/Ag_2O immobilized on cellulose paper: A new floating system for enhanced photocatalytic and antibacterial activities. *Environ. Res.* **198**, 111257. https://doi.org/10.1016/j.envres.2021.111257 (2021).
66. Wu, T., Liu, G., Zhao, J., Hidaka, H. & Serpone, N. Photoassisted degradation of dye pollutants. V. Self-photosensitized oxidative transformation of rhodamine B under visible light irradiation in aqueous TiO_2 dispersions. *J. Phys. Chem. B.* **102**, 5845–5851 (1998).
67. Li, J. Y., Ma, W. H., Lei, P. X. & Zhao, J. C. Detection of intermediates in the TiO_2-assisted photodegradation of Rhodamine B under visible light irradiation. *J. Environ. Sci. (China)* **19**, 892–896 (2007).
68. Cui, Y., Goldup, S. M. & Dunn, S. Photodegradation of Rhodamine B over Ag modified ferroelectric $BaTiO_3$ under simulated solar light: Pathways and mechanism. *RSC Adv.* **5**, 30372–30379 (2015).
69. Chiu, Y.-H., Chang, T.-F.M., Chen, C.-Y., Sone, M. & Hsu, Y.-J. Mechanistic insights into photodegradation of organic dyes using heterostructure photocatalysts. *Catalysts* **9**, 430 (2019).
70. Chokesawatanakit, N. *et al.* Enhancing the multifunctional properties of cellulose fabrics through in situ hydrothermal deposition of TiO_2 nanoparticles at low temperature for antibacterial self-cleaning under UV–Vis illumination. *Int. J. Biol. Macromol.* **256**, 128321. https://doi.org/10.1016/j.ijbiomac.2023.128321 (2024).

Acknowledgements

This research project is supported by National Research Council of Thailand (NRCT): NRCT**5**-RGJ**63**003-053. Such a funding is hereby gratefully acknowledged. Also, this research work is supported by Research and Graduate Studies, Khon Kaen University.

Author contributions

N.P. conducted all experiments, performed characterization, and prepared and wrote the main manuscript. S.T. contributed to the writing of the main manuscript text and provided suggestions. K.K. was involved in conceptualization, and reviewed, checked, and corrected the main manuscript text.

Competing interests
The authors declare no competing interests.

Additional information
Correspondence and requests for materials should be addressed to K.K.

Reprints and permissions information is available at www.nature.com/reprints.

Publisher's note Springer Nature remains neutral with regard to jurisdictional claims in published maps and institutional affiliations.